修士論文

Electric Field Dependence of Photoluminescence from Single-Walled Carbon Nanotubes

単層カーボンナノチューブにおける フォトルミネッセンスの電界変調効果

指導教官　　加藤雄一郎　准教授

東京大学大学院工学系研究科電気系工学専攻

学籍番号　　37-096510

氏名　　安河内　諭

Abstract

Semiconducting single-walled carbon nanotubes are a promising material for applications in photonics and optelectronics, because of their direct band gap and one dimensional structure. In this work, using suspended single-walled carbon nanotubes, electric field effects on photoluminescence is investigated. It is expected that energy shifts would be caused by screening effects due to doped carriers by the electric field. In order to allow an application of electric fields on as-grown nanotubes, back-gated field effect transistors are used. Trenches are fabricated on SiO_2/Si substrates, and Pt is deposited for electrical contacts. Carbon nanotubes are grown by patterned chemical vapor deposition. Individual suspended carbon nanotubes are identified by taking photoluminescence images using a home-built laser-scanning confocal microscope. After determining the chirality by photoluminescence excitation spectra, we measure the gate voltage dependence on photoluminescence. We observe quenching of photoluminescence intensity and blue shifts of emission wavelength as gate voltages are applied. Screening effects are not observed. A possible cause of the energy shifts is migration of adsorbed molecules due to the electric field. Theoretical calculation of the photoluminescence quenching caused by the increase of scattering with carriers is compared with experimental results.

Acknowledgments

During the two years of master's course, I have enjoyed the time in my group and conducted my study thanks to a lot of people. First of all, I am deeply grateful to my supervisor Prof. Yuichiro Kato for his continued advice and valuable discussion about my research. I would also like to express my gratitude to Dr. Takashi Shimada for many advice about device processes and CVD growth. I would like to thank to Tomoaki Murai and Shigeru Moritsubo for teaching me how to use measurement systems and equipments for device fabrication. Yoshifumi Horiuchi and Satoshi Harashima as the students in the same grade have shared joys and sorrows with me. Ryosuke Watahiki, Masahiro Yoshida and Akio Yokoyama offered opportunities to enjoy exercise and sports. I hope Tatsuya Horiguchi and Akihiro Ishii complete their bachelor work. I would like to give special thanks to Dr. Shohei Chiashi in Maruyama group for useful advice and providing use of SEM or CVD system. I also would like to thank to Dr. Tetsuo Kan in Simoyama group for the support in E-beam evaporation. I am grateful to Dr. Masanori Kubota for giving precious advice about device processes and teaching how to use several facilities in Takeda CR. Finally, I would like to show special gratitude to my family for continued support.

Contents

Chapter 1 Introduction

1.1 Background

Carbon nanotubes (CNTs),which are hollow cylinders composed of carbon atoms discovered in 1993[1], have a lot of outstanding properties, such as high electron mobility, high current density and mechanical toughness[2][3]. Single-walled carbon nanotubes (SWCNTs) change their band structure depending on chirality, and can be metallic and semiconducting. Semiconducting SWCNTs are promising materials in nano-optelectronics, because they have direct band gap corresponding to infrared range, and small diameter of ∼1nm. Since the first observation of fluorescence from SWCNTs[4], optical properties of SWCNTs have been investigated intensely. Various CNT devices, such as field effect transistors (FETs)[5][6], light emitting diodes (LEDs)[7][8][9][10] and photo detectors are reported[11].

In SWCNTs, Coulomb interaction of carriers is very strong, because they are confined into narrow one-dimensional structure. Therefore existence of excitons which are pairs of electrons and holes was predicted by theoretical calculation in 1997[12]. It was experimentally demonstrated that excitons could be stable and have large binding energy by two photon excitation spectroscopy in 2005[13], which indicated excitons played a critical role in optical processes. Excitons are very important in order to understand optical properties of SWCNTs. These days physical properties of excitons in SWCNTs are studied intensely, such as lifetime and diffusion length of excitons[14][15], exciton dynamics and irradiative excitonic states (dark excitons)[16].

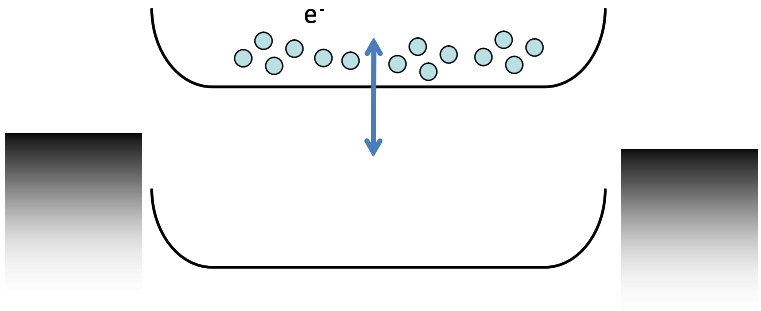

Fig. 1.1.1: A schematic of SWCNT band structure modulated by electric field.

1.2 Focus of the thesis

Optical properties of SWCNTs is dominated by recombination of excitons. Luminescence from SWCNTs are modulated by changing Coulomb interaction of carriers. Therefore, it is expected that light emission from SWCNTs can be controlled by external electric field. It is reported that emission wavelength is shifted in air-suspended SWCNTs compared with micelle-wrapped SWCNTs[17][18]. This is caused by a difference of dielectric constant between air-suspended SWCNTs and micelle-wrapped SWCNTs. In a similar way, emission wavelength could be shifted by changing carrier density in SWCNTs generated by external electric field as shown in Fig. 1.1.1.

There are several reports with respect to electric field dependence of photoluminescence (PL)[19][20][21]. Although PL quenching by electric field is observed, photon energy shift of PL is not identified yet. In addition, it is also indistinct why PL intensity is drastically decreased. Therefore electric field effect on SWCNTs remains a matter of research. In this study, electric field dependence of PL was investigated from SWCNTs, in particular, which are identified their chirality and confirmed that they are individual.

1.3 Organization

This thesis is organized as follows. Chapter 2 gives an overview about previous studies on optical properties of SWCNTs. Electronic structure, PL measurement, and exciton features are mainly explained. Chapter 3 contains the experimental methods for device fabrication, electrical properties of devices, and characterization of SWCNTs. Result and discussion of electric field dependence of PL is presented in Chapter 4. The experiments and results are summarized in Chapter 5.

Chapter 2 Physical properties of single-walled carbon naotubes

2.1 Electronic structure of single-walled carbon nanotubes

2.1.1 Lattice structure of single-walled carbon nanotubes

CNTs are obtained by rolling up a single graphite layer (a graphene sheet), hexagonal lattice made up of carbon atoms as shown in Fig. 2.1.1. There are various kinds of CNTs depending on rolling up directions. CNTs composed of a single graphene layer are called single-walled carbon nanotubes (SWCNTs), and those composed of a number of layers are called multi-walled carbon nanotubes (MWNTs). Only SWCNTs is covered in this thesis.

Points A and B in Fig. 2.1.1 correspond to each other when rolling up a graphene sheet. The line connecting points A and B corresponds to circumference of a SWCNT, and $\overrightarrow{\mathrm{AB}}$ is called chiral vector $\boldsymbol{C_h}$. $\boldsymbol{C_h}$ can be represented using unit lattice vectors $\boldsymbol{a_1}$ and $\boldsymbol{a_2}$ in a graphene sheet as follows.

$$\boldsymbol{C_h} = n\boldsymbol{a_1} + m\boldsymbol{a_2} \equiv (n, m) \tag{2.1.1}$$

where n, m are integers satisfying $0 \leq m \leq n$. A pair of coefficients (n, m) is called chiral index (or chirality). Structures of SWCNTs are determined by chirality. In particular, SWCNTs with (n, n) or $(n, 0)$ chiral index are called armchair or zigzag nanotubes, respectively, from their cross-sectional configuration of carbon atoms. Lattice structures of these two types of SWCNTs are identical to their mirror images, also called achiral nanotubes. In contrast other SWCNTs which are not identical to their mirror images are called chiral nanotubes.

Diameter d_t of SWCNTs can be represented using the chiral vector $\boldsymbol{C_h}$ as follows.

$$d_t = \frac{|\boldsymbol{C_h}|}{\pi} = \frac{a}{\pi}\sqrt{n^2 + nm + m^2} \tag{2.1.2}$$

where a is lattice constant. $\overrightarrow{\mathrm{AC}}$, called the translation vector $\boldsymbol{T}$, is defined as the vector normal to $\boldsymbol{C_h}$, which starts at A and terminates at the first lattice point C.

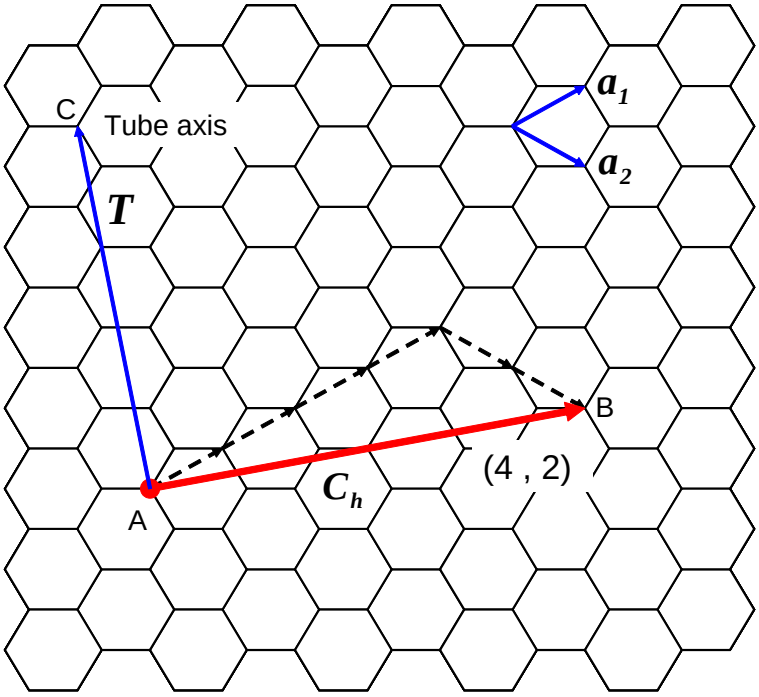

Fig. 2.1.1: The unrolled hexagonal lattice of a SWCNT.

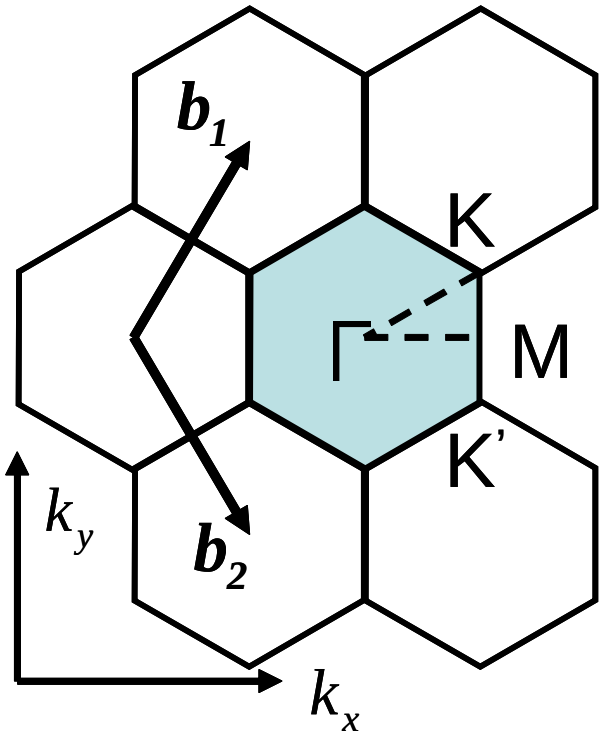

Fig. 2.1.2: Brillouin zone of graphene.

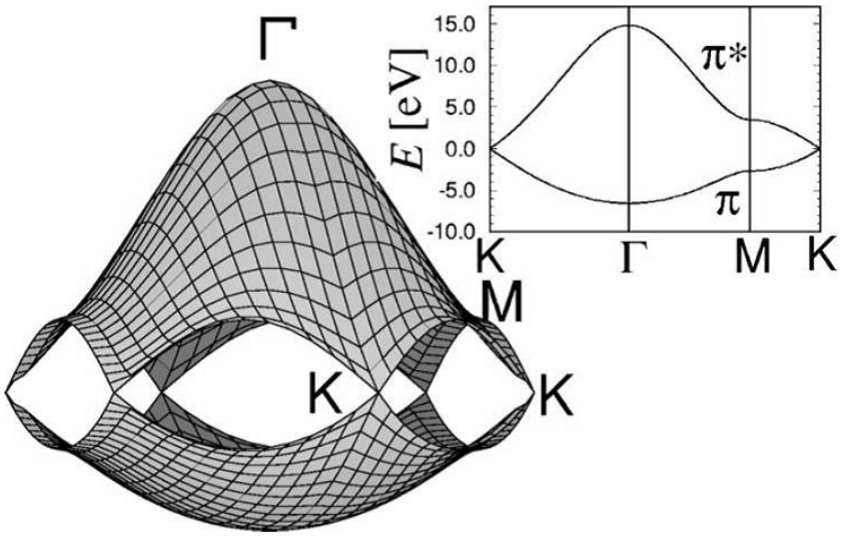

Fig. 2.1.3: The energy dispersion relations for graphene[22]. The inset shows the energy dispersion along the high symmetry directions of the triangle ΓMK shown in Fig. 2.1.2.

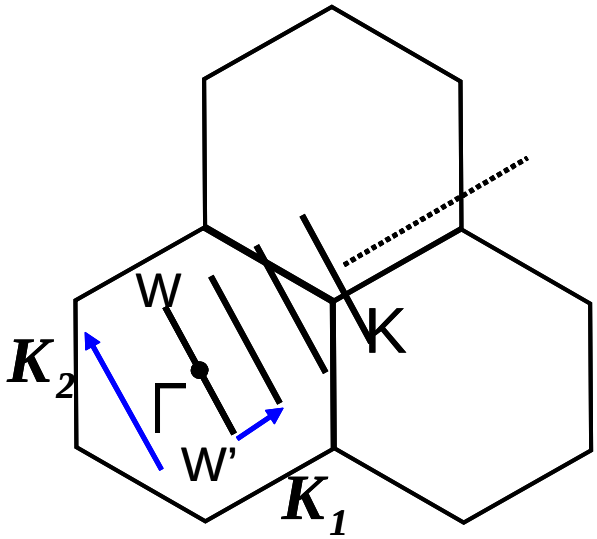

Fig. 2.1.4: The Brillouin zone of a SWCNT.

The lattice structure is periodic under translation T. The unit cell of a SWCNT is a rectangle defined by $\boldsymbol{C_h}$ and $\boldsymbol{T}$.

2.1.2 Band structure of graphene

Band structure of SWCNTs can be obtained by imposing on periodic boundary condition in the direction of $\boldsymbol{C_h}$. Therefore, firstly electronic structure of graphene is considered. The unit cell of graphene is a diamond shape defined by $\boldsymbol{a_1}$ and $\boldsymbol{a_2}$ in Fig. 2.1.1. Fig. 2.1.2 shows the reciprocal lattice of graphene. $\boldsymbol{b_1}$ and $\boldsymbol{b_2}$ are its unit vectors. Therefore, the Brillouin zone of graphene is a region defined by $\boldsymbol{b_1}$ and $\boldsymbol{b_2}$, which is the blue-colored hexagon. The center, vertices and mid points of sides in this hexagon are called Γ, K(K′) and M point respectively. K and K′ are two quivalent corners. The energy band of graphene E_{2g} can be obtained as follow using tight binding calculation which considers only $2p_z$ orbital.

$$E_{2g} = \frac{\epsilon_{2p} \pm \gamma_0 w(\boldsymbol{k})}{1 \pm s w(\boldsymbol{k})}, \tag{2.1.3}$$

$$w(\boldsymbol{k}) = \sqrt{e^{ik_x a/\sqrt{3}} + 2e^{-ik_x a/2\sqrt{3}} \cos\frac{k_y a}{2}}, \tag{2.1.4}$$

where ϵ_{2p} is the energy of $2p_z$ orbital, and s is the overlap integration of two nearest carbon atoms. Fig. 2.1.3 shows the energy dispersion relations for graphene given by Eq. 2.1.3. The upper energy band is the π anti-bonding and the lower one is the π bonding band. It is found that the conduction band and the valence band are degenerate at K and K′. Therefore, graphene behaves as a zero gap semiconductor or semi-metal.

2.1.3 Band structure of single-walled carbon nanotubes

Electronic structure of SWCNTs is calculated by quantizing energy band of graphene obtained previously, in the direction of circumference of SWCNTs. The reciprocal lattice vectors $\boldsymbol{K_1}$ and $\boldsymbol{K_2}$ in the unit cell of SWCNTs defined by $\boldsymbol{C_h}$ and $\boldsymbol{T}$ is given by following equation.

$$\boldsymbol{C_h} \cdot \boldsymbol{K_1} = 2\pi, \boldsymbol{T} \cdot \boldsymbol{K_1} = 0, \tag{2.1.5}$$

$$\boldsymbol{C_h} \cdot \boldsymbol{K_2} = 0, \boldsymbol{T} \cdot \boldsymbol{K_1} = 2\pi. \tag{2.1.6}$$

In addition, the wave number vector in the circumferential direction $\boldsymbol{k}$ satisfies the following periodic boundary condition.

$$\boldsymbol{C_h} \cdot \boldsymbol{k} = 2\pi i (i = 0, 1, 2 \dots) \tag{2.1.7}$$

As the result, the Brillouin zone of SWCNTs as shown in Fig. 2.1.4 is obtained. The Brillouin zone of SWCNTs is lines which are formed by moving WW, to $\boldsymbol{K_1}$. Therefore the energy dispersion relations for SWCNTs are given by the following equation.

$$E_\mu = E_{2g}(k\frac{\boldsymbol{K_2}}{|\boldsymbol{K_2}|} + \mu\boldsymbol{K_1}) \tag{2.1.8}$$
$$(\mu = 0, 1 \ldots N-1, -\frac{\pi}{|\boldsymbol{T}|} \leq k \leq \frac{\pi}{|\boldsymbol{T}|}).$$

N bonding π bands and anti-bonding π^* bands are obtained respectively. The lines of the Brillouin zone of SWCNTs are also called cutting lines. When cutting lines include the K points, these SWCNTs become zero gap semiconductors (metallic tubes). When cutting lines don't pass K points, these SWCNTs have band gaps and behave as semicondutors. The condition where cutting lines pass K points is equivalent to the following equation.

$$n - m \equiv 0 \pmod 3 \tag{2.1.9}$$

2.1.4 Density of states and selection optical rules in single walled carbon nanotubes

The density of states (DOS) of SWCNTs is very different from other bulk semiconductor, since they are one dimensional materials. Fig. 2.1.5 shows the DOS of semiconducting SWCNTs and the general bulk semiconductors, respectively. The solid line indicates the DOS of SWCNTs, and dash the one shows bulk semiconductor. While the DOS of bulk semiconductor monotonically increases in proportion to $\sqrt{E}$, the DOS of SWCNTs have peaks at certain points. This is because DOS diverges at the points where $2N$ SWCNT bands reach external values ($\partial E(k)/\partial k = 0$). DOS diverges asymmetrically proportionally to $1/\sqrt{E - E_i}$. (E_i is an external value.) These points are called van Hove singularities. When optical transitions, such as light absorption or emission, occur between van Hove singularities, intensity of the transition becomes very large due to the divergence of the DOS. v_i and c_i in Fig. 2.1.5 denote the van Hove singularities in valence bands and conduction bands. v_i and c_i are put into numerical order from band gap.

Optical response of SWCNTs to light polarized parallel to tube axis is extremely different from that to perpendicular one because of the one dimensional structure. In the case that parallel polarized light is shined on SWCNTs, only $v_i c_i$ symmetric transition occures. In contrast, when perpendicularly polarized light is shined, $v_i c_{i\pm1}$ transition is allowed. Moreover, the transition caused by perpendicularly polarized light is suppressed since polarization generated in SWCNTs cancel out the optical

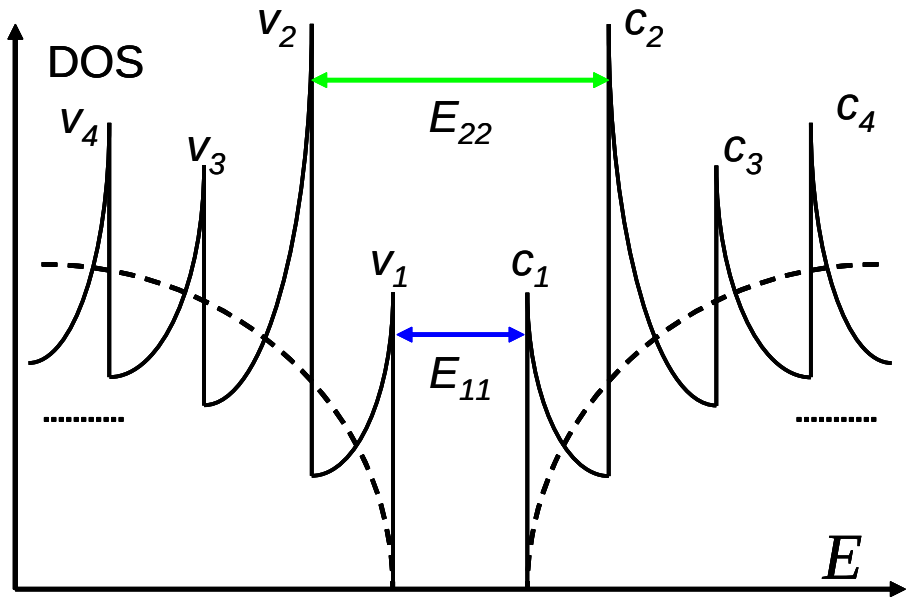

Fig. 2.1.5: Electronic density of states (DOS) for a semiconducting SWCNT (solid line) and bulk semiconductor (dash line).

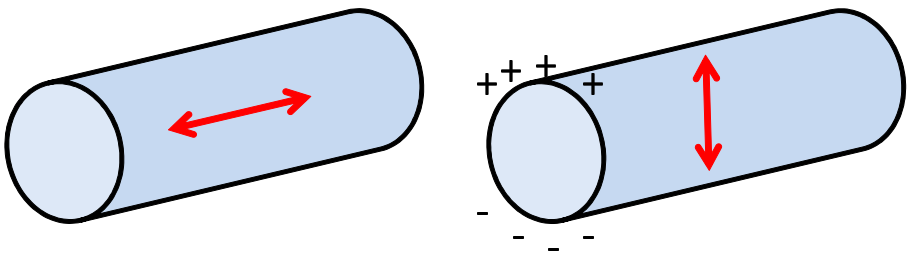

Fig. 2.1.6: Schematic of polarized light parallel (left) and perpendicular (right) to tube axis. In case of perpendicular electric field, polarization charge is generated.

electric field. (depolarization effect)[23] Experimentally, absorption of perpendicularly polarized light is extremely smaller than that of parallel light[24][25]. Therefore $v_i c_i$ transition mainly occurs in SWCNTs.

2.2 Photoluminescence from single-walled carbon nanotubes

2.2.1 Observation of fluorescence from single-walled carbon nanotubes

In the early stage, optical properties of SWCNTs were studied mainly using Raman spectroscopy and absorption spectroscopy. In particular Raman scattering is generally used in order to measure diameter of SWCNTs since the radial breathing mode (RBM), a vibration mode in the diameter direction of SWCNTs, is proportional to the inverse of tube diameter.

Attempts to observe fluorescence from semiconducting SWCNTs was intensely done from the beginning, since they were direct band gap semiconductor. However light emission from grown SWCNTs could not be observed for a long time, although resonant Raman scattering could be observed. This is mainly because as-grown SWCNTs aggregate and form bundles owing to quite strong van der Waals interaction between SWCNTs. Since the bundles are composed of metallic and semiconducting SWCNTs, irradiative recombination of generated electron hole pairs occurs in metallic SWCNTs. Therefore, in order to observe fluorescence from SWCNTs, they need to be isolated.

O'Connell *et al.* have observed photoluminescence (PL) from semiconducting SWCNTs in 2002 for the first time by encapsulating SWCNTs with surfactant to

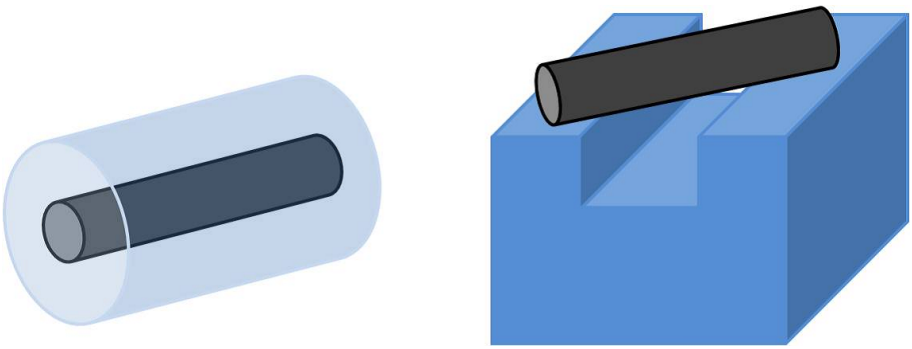

Fig. 2.2.1: A schematic of a SWCNT encapsulated with surfactant (left) and suspended over a trench (right).

form micelles as shown in Fig. 2.2.1[4]. Aqueous solutions of SWCNTs and sodium dodecyl sulfate (SDS) were sonicated and centrifugated, leading to isolated individual SWCNTs wrapped with SDS. Several PL peaks are observed from SDS-wrapped SWCNTs in heavy water (D_2O) within the near infrared region and accurately overlapped with absorption peaks. These distinct emission peaks are attributed to electronic transitions of E_{11} in different SWCNT species.

They also investigated excitation wavelength dependence of PL from a SWCNT of certain chirality. It turns out that the PL intensity has local maximum value at specific laser wavelength. This is caused by the DOS of SWCNTs which has many spikes as shown in Fig. 2.1.5. When photon energy of the laser corresponds with that of transitions between van Hove singularities, absorption of photon is enhanced. Excited electron and hole pairs relax into the lowest excited state E_{11}, leading to radiative recombination as shown in Fig. 2.2.2. Therefore, the intensity of PL from SWCNTs has the excitation energy dependence.

2.2.2 Chirality assignment by photoluminescence excitation spectroscopy

Bachilo *et al.* made assignment of chirality in SWCNTs by using the excitation energy dependence of PL intensity[27]. PL intensity is strongly enhanced when excited with E_{ii} energy. As a result, values of E_{11} and E_{22} can be obtained. Comparing this PLE map with theoretical calculation, values of E_{11} and E_{22} in various chirality of SWCNTs can be determined. They also presented empirical Kataura plot where E_{ii} plotted as a function of tube diameter from this obtained data[28]. It is reported that both E_{11} and E_{22} in empirical Kataura plot is lager than theoretical values. They attributed this energy difference to trigonal warping, curvature and exciton binding[29][30][31]. The empirical Kataura plot is widely used for assignment of chiral indices for semiconducting SWCNTs.

2.2.3 Air-suspended individual single-walled carbon nanotubes

Recently, chemical vapor deposition (CVD), which is one of the most popular synthesis methods of SWCNTs, is frequently used to directly grow SWCNTs on substrates[34][35]. Various devices have been fabricated using CVD since this method offers a convenient way to obtain non-bundled and oriented SWCNTs position-controlled by lithography. However PL can not be observed from SWCNTs directly touching substrates such as silicon and quartz). In order to avoid the substrate-induced quenching of PL, SWCNTs need to be suspended over pillars and trenches fabricated on substrates as shown in Fig. 2.2.1.

Lefebvre *et al.* observed PL from air-suspended SWCNTs in 2003 first[32]. Arrays of pillars were fabricated on silicon substrate, and a thin layer of iron and cobalt as catalyst was deposited by electron beam evaporation. Finally, SWCNTs were grown by methane CVD at between 800°C and 900°C . Strong and narrow PL peaks were observed from suspended SWCNTs over the pillars. No detectable light, however, was observed from SWCNTs on the substrate. This fact indicated that the PL peaks were thought to be from suspended SWCNTs.

They also measured PL from suspended individual SWCNTs using this method[33]. The full width at half maximum value of the peak is typically about 10 meV, which is smaller than that of micelle-wrapped SWCNTs ensemble (about 25 meV [4])The lineshape of the peak is asymmetric, because of the shape of the von Hove singularities peaks in the DOS of SWCNTs.

2.3 Excitons in single-walled carbon nanotubes

2.3.1 Effect of excitons in single-walled carbon nanotubes

In addition to von Hove singularities, excitons play a important role in optical process in one-dimensional systems. Generally, an electron and a hole form a bound state by Coulomb interaction such as a hydrogen atom. This bound state is called an exciton. The binding energy of excitons becomes lager as dimensionality of a system become lower, leading excitons to be more stable. In 1997, Ando *et al.* theoretically predicted that the effect of excitons prominently appeared in SWCNTs[12]. They reported that band gap became lager when Coulomb interaction was taken into account. Fig. 2.3.1 shows schematic band gap with or without the Coulomb interaction. E_{SP} is bad gap calculated by single-particle theories which do no consider the Coulomb interactions. E_{11}^{b} denotes a discrete exciton state, corresponding to the lowest excited state. E_{11}^{∞} shows continuum states. There are two types of contributions in the Coulomb interactions between carriers. One is self-energy correction Σ, which arises from the repulsive Coulomb interaction between electrons. This effect lifts up the continuum states and increases the band gap value. The other is the attractive Coulomb interaction between electrons and holes, which generates various excitonic states below the continuum sates and decrease the band gap by the amount of binding energy E_b. Therefore the values of E_{11}^{∞} and E_{11}^{b} are expressed as follows.

$$E_{11}^{\infty} = E_{SP} + \Sigma \tag{2.3.1}$$

$$E_{11}^{b} = E_{11}^{\infty} + \Sigma - E_b \tag{2.3.2}$$

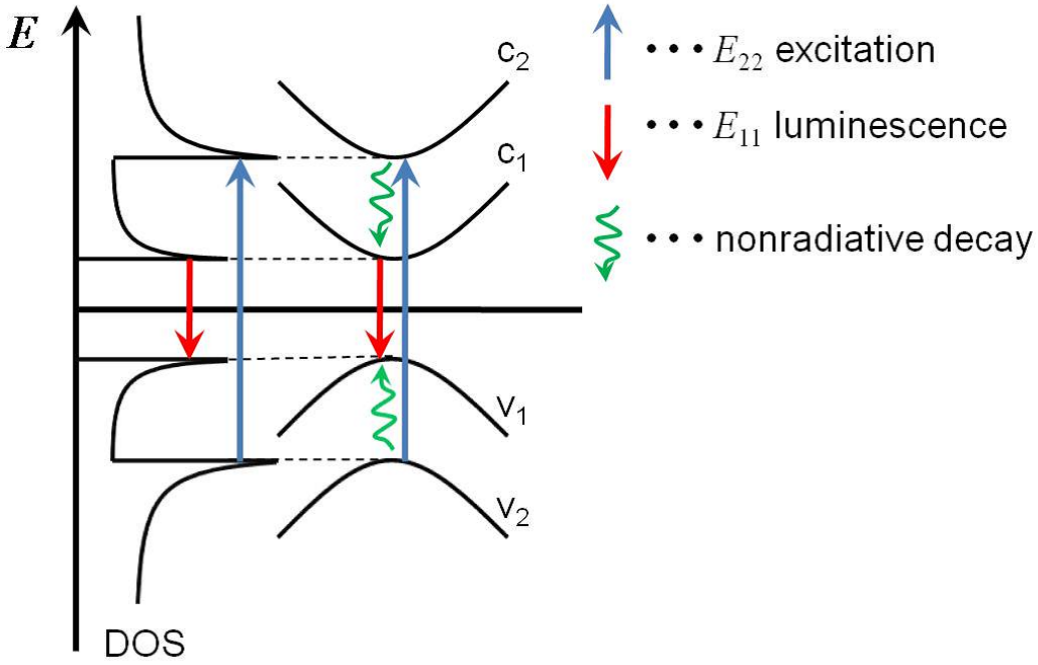

Fig. 2.2.2: A schematic of PL process. Taken from [26].

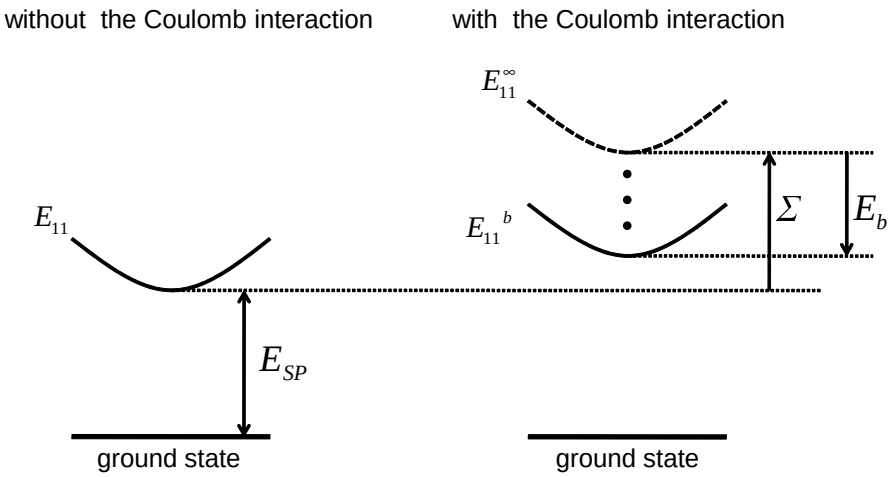

Fig. 2.3.1: Change of the band gap due to the Coulomb interaction. Adapted from [26].

Since Σ is somewhat larger than E_b, E_{11}^b energy is blue-shifted from the single-particle band gap E_{SP}. On the other hand, E_{22} is not changed so much since Σ is comparable to exciton binding energy in E_{22}.

This blue shift can also explain the absorption spectrum of SWCNTs[31]. It was known that the measured absorption spectra is blue-shifted from those calculated using tight binding model. This experimental fact implied that excitons in SWCNTs have a critical role in optical transitions, since this blue shift is consistent with Ando's report.

2.3.2 Demonstration of existence of excitons and binding energy

Existence of excitons was demonstrated using two-photon excitation spectroscopy in 2005[13]. In two-photon excitation, an electron is excited absorbing two-photons whose energy correspond to an half of the transition energy. Optical selection rule for two-photon excitation is different from those for one-photon excitation. In one photon excitation, transitions from odd states, whose wave function is odd function, to even states are allowed. In contrast, two-photon excitation allows transitions from odd (even) states to odd (even) states. Fig. 2.3.2 shows a schematic of band structure of SWCNTs in the exciton picture and the band picture. In the exciton picture, the bound excitonic states are generated, same as hydrogen atoms. In the exciton picture, an electron is excited to the $2g$ state, which is prohibited in one photon excitation, from the ground state. The electron relaxes into the $1u$ state and emits light. Therefore excitation energy is different from emission energy in the exciton picture. In the band picture, however, The emission energy is the same as the excitation photon energy as shown in Fig. 2.3.2. Two-photon excitation spectra are measured from SWCNTs prepared as shown in [4]. It is reported that emission energy is smaller than excitation energy in all measured SWCNTs. Therefore this result is in good agreement with the exciton picture.

2.3.3 Exciton binding energy

J. Maultzsch *et al.* also measured two-photon excitation spectra and compared it with one-photon excitation spectra[36]. It is reported that a peak in the one photon excitation spectrum was observed below the peak of E_{11}^g in the two-photon excitation spectrum. This peak arises from $2u$ transition, and this result is consistent with the exciton picture in Fig. 2.3.2. The energy difference between the $1u$ state and the $2g$ state, which can be considered comparable to exciton binding energy, is estimated at

240 meV. This result indicates that excitons in SWCNTs exist stably and dominate the optical properties.

Diameter dependence of the exciton binding energy is also investigated [37]. It is found that exciton binding energy is proportional to the inverse of tube diameter.

2.3.4 Effect of dielectric screening

The strength of the Coulomb interactions between carriers in SWCNTs depends on the dielectric constant of surrounding materials as well as that of SWCNTs themselves, since large amounts of electric flux pass through the outside of the tube[38][39]. As a consequence, the E_{11} and E_{22} energies are affected by the surrounding environment.

Since the first observation of PL from air-suspended SWCNTs, severall studies have reported blue-shifts about 10-30 meV for both the E_{11} and E_{22} energies of air-suspended SWCNTs compared to the values of micellle-wrapped SWCNTs[17][18][40]. These shifts are explained by the enhanced Coulomb interactions caused by the reduced dielectric screening for air-suspended SWCNTs because the dielectric constant of air-suspended SWCNTs is thought to be smaller than that of micelle-wrapped SWCNTs. Coulomb interaction For most species of SWCNTs, the increase of the electron-electron repulsive energy Σ is larger than that of the electron-holes binding energy E_b, leading to total blue-shifts. Also, SWCNTs of some chirality showed redshift of E_{22} energy[18], suggesting the reversed amplitude of the changes of the repulsive energy and the binding energy for some species of SWCNTs.

Several reports studied the effect of dielectric screening by systematically varying the dielectric constant with changing humidity for trench-suspended SWCNTs or immersing trench-suspended SWCNTs into various organic solvents[41][42]. Similar blue-shifts were observed in both experiments and confirmed the above picture.

Recently, it was revealed that atmospheric molecules adsorbs on the surface of trench-suspended SWCNTs under the ambient conditions. By heating the SWCNTs high laser irradiation, or placing then under high-vacuum conditions, the molecules are desorbed from the SWCNTs and the dielectric constant is decreased[43]. This results in sudden blue-shifts of E_{11} and E_{22} values, called band gap shift transition.

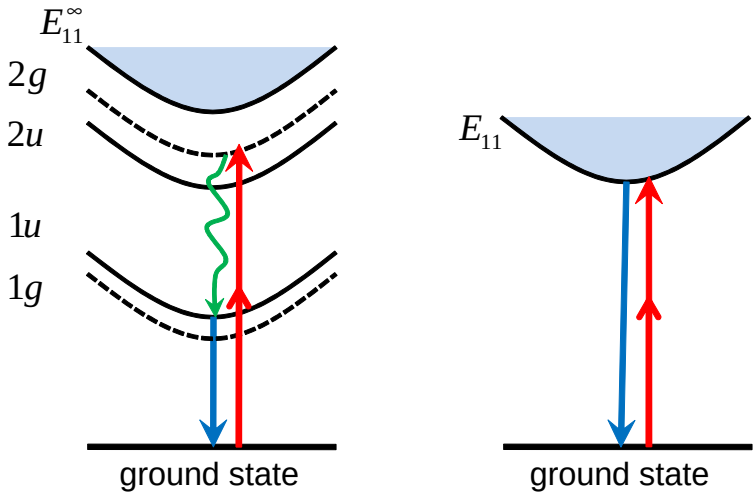

Fig. 2.3.2: Schematic band structure of a SWCNT in the exciton picture (left) and the band picture (right).

Chapter 3 Device fabrication and characterization

3.1 Device fabrication

In order to investigate electric field dependence of photoluminescence, air-suspended individual SWCNT field effect transistors (FETs) as shown Fig. 3.1.1 were fabricated. The suspended structure was fabricated because SWCNTs need to be isolated for observation of PL. Widths of trenches were about 1 μm . Widths of electrode were 10 μm . Fabrication process is described below.

Fabrication of trenches

- Patterning of trenches

  OAP and ZEP520A (e-beam resist) were spincoated on a substrate, a 4 inch silicon wafer ((100) surface) with 100 nm thickness silicon dioxide. The spincoating condition is after 500 rpm for 5 seconds 4000 rpm for 60 seconds. After spincoating, the substrate was baked at 180°C for 15 minutes on a hot plate. Trenches were patterned on this substrate using electron beam (e-beam) lithography (ADVANTEST, F5112). Dose amount is 104 C/cm^2. Exposed sample was developed by ZED-N50 for 1 minutes, and rinsed in ZMD-B. After devlopment, the wafer was baked at 180°C for 4 minutes to make more tolerant to etching.

- Etching process

  First, SiO_2 layer on patterned sample was etched using buffered hydrofluoric acid (BHF). Etching time is 65 seconds. After that, the wafer was rinsed in water. Secondly, silicon layer was etched by inductively-coupled plasma (ICP) etcher (AMS100) for one minute. Width and depth of trenches are about 1 μm and 5 μm respectively. Finally, e-beam resist was removed by sonication in Hakuri104 (Tokyo Ohoka) and rinsed in isopropyl alcohol (IPA).

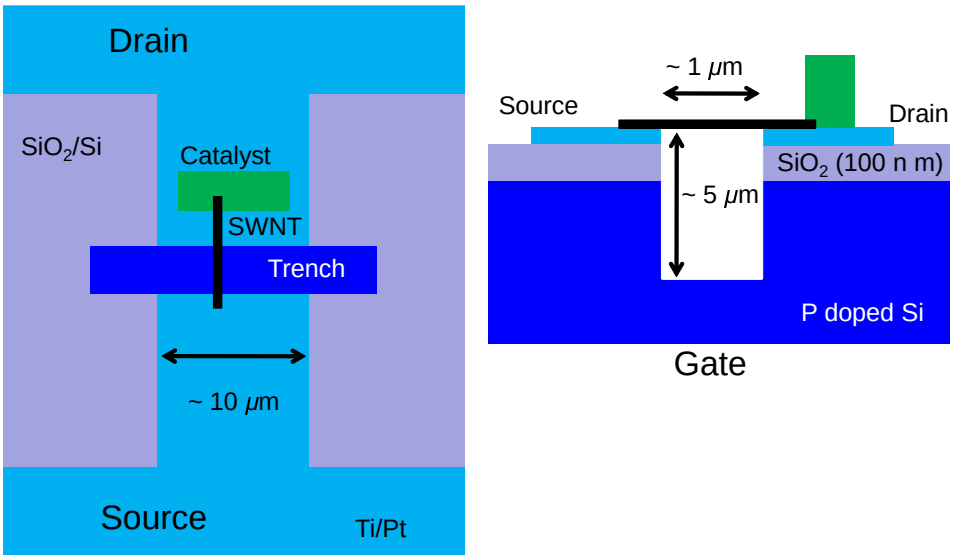

Fig. 3.1.1: Schematic of trench-suspended individual SWCNT FET. Top view (left) and cross-section (right).

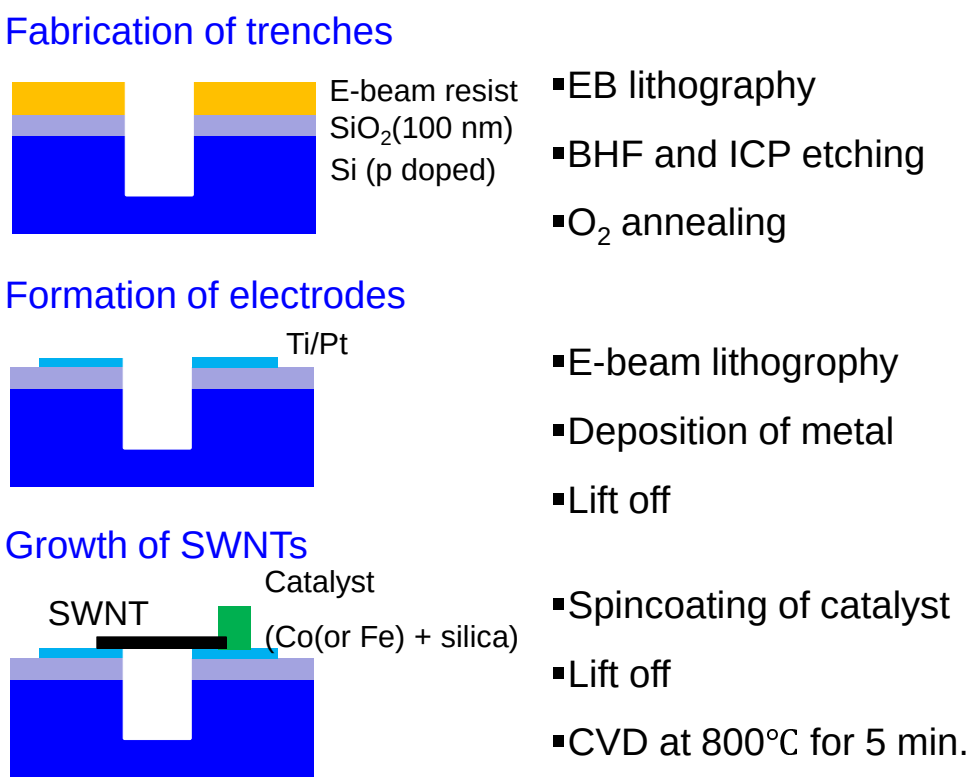

Fig. 3.1.2: Device fabrication steps.

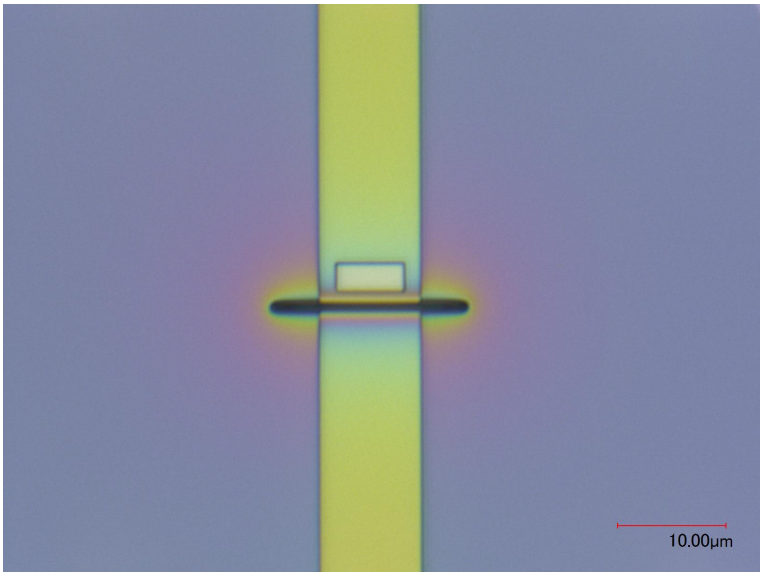

Fig. 3.1.3: Optical image of the catalyst pattern

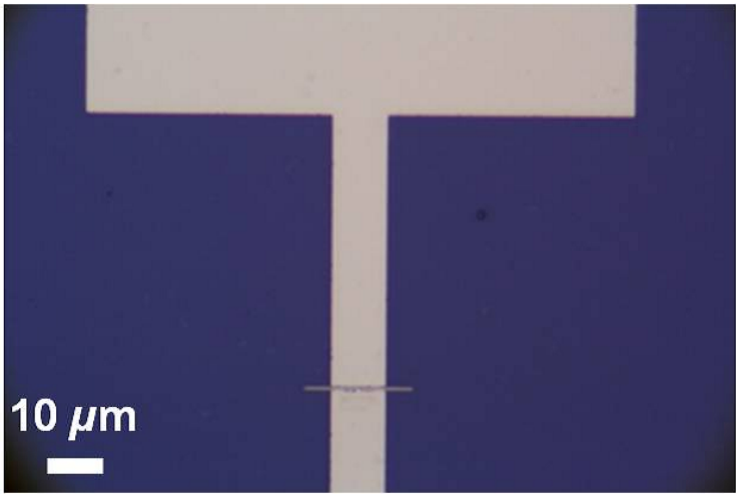

Fig. 3.1.4: Optical image of the fabricated device after CVD growth.

- Annealing

  After fabrication of trenches, the wafer was annealed in order to insulate the surface of trenches. This process is important to prevent gate leakage in devices. The sample was annealed in the diffusion furnace at 900°C for an hour flowing 1.5 L/min O_2. Thickness of SiO_2 at the side wall of trenches is about 16 nm.

Deposition of electrodes

- Patterning of electrodes

  E-beam resist was spincoated on the samples the same way as patterning of trenches. Instead of ZEP520A, OEBR CAP-112PM which is thicker and more tolerant to heat was used. OAP was spincoated at 3000 rpm for 30 seconds, and the sample was baked at 110°C for 60 seconds. Next, OEBR was deposited at 2500 rpm for 60 seconds. Finally, the sample was baked for 5 minutes at 110°C . After exposure in dose 7 C/cm^2, the wafer was baked for 2 minutes at 110°C (post exposure bake process). The pattern was developed in Tetramethyl ammonium hydroxide (TMAH) for 70 seconds, and rinsed in water.

- Deposition of metal

  Metal for electrodes was deposited by E-beam evaporation (ULVAC, EX400) in Shimoyama Lab. The sample wafer was cleaved to 2cm $\times$ 2cm chips because the mounts of the chamber was small. Firstly 1 nm Ti was deposited on the sample as an adhesive layer. Deposition rate is 0.1 nm/s. In the next step, 15 nm Pt was deposited as electrodes at the rate of 0.05 nm/s.

- Lift off and cleaning process

  For formation of electrodes, E-beam resist was removed. The sample was soaked in Hakuri104 for one day, and rinsed by IPA. Remaining resist was ashed by O_2 plasma for about 2 minutes. Finally, the sample was cleaned by sonicating in acetone for 5 minutes.

Growth of single-walled carbon nanotubes

- Patterning of catalyst

  OAP and ZEP520A are spincoated on the chip. Spincoating condition is the same as trench patterning. The sample was baked at 180°C for 5 minutes. After exposure, catalyst pattern is developed in the similar way of trench patterning. In this patterning, the sample was not postbaked. Fig. 3.1.3 shows an optical microscope image of the catalyst patterned sample.

- Preparation and deposition of catalyst

  Firstly, catalyst solution was prepared. Cobalt acetate or iron acetate as catalyst and fumed silica as supported material were dissolved in ethanol. Typical condition of preparation is 16.9 mg of cobalt and 200 mg of silica in 80 g ethanol. This solution was sonicated for one hour.

  Catalyst solution was spincoated on the sample chip at 3000 rpm for 50 seconds. Amount of the solution is 50 μl per 10 mm$\times$ 10 mm chip. After 5 minutes, the sample was baked at 80°C for 5 minutes. Then the sample was dipped in Hakuri104 to dissolve the resist and lift off extra catalyst. Finally, the sample was heated up in a furnace at 400°C for 5 minutes in order to remove and decompose the organic molecules such as e-beam resist and form oxide of catalyst metal.

- Growth of single-walled carbon nanotubes by chemical vapor deposition

  Fig. 3.1.6 shows a schematic of the CVD sytem. A quartz tube with 1 inch diameter, in which samples are placed, is installed in an electrical furnace. By evacuating the tube with a vacuum pump connected to the downstream of the tube, Ar/H_2, whose flow rate is regulated by mass flow controller, ethanol vapor can be led into the tube. A needle valve is used to control the pressure in the tube. The CVD growth was conducted as follows.

  Firstly, the sample, which was placed on a quartz boat, was transferred into the quartz tube and the temperature was elevated to 800°C in 30 minutes in vacuum. In this heating process, 300 sccm of Ar/H_2 gas was delivered and the pressure in the tube was maintained at 40 kPa, leading to reduction of the catalyst metal oxide into activated nanoparticles supported on the fumed silica. After reaching 800°C , the gas supply was stopped and the pressure was decreased to about 0.1 Pa. Then ethanol vapor was led into the tubes as carbon source. The growth process was

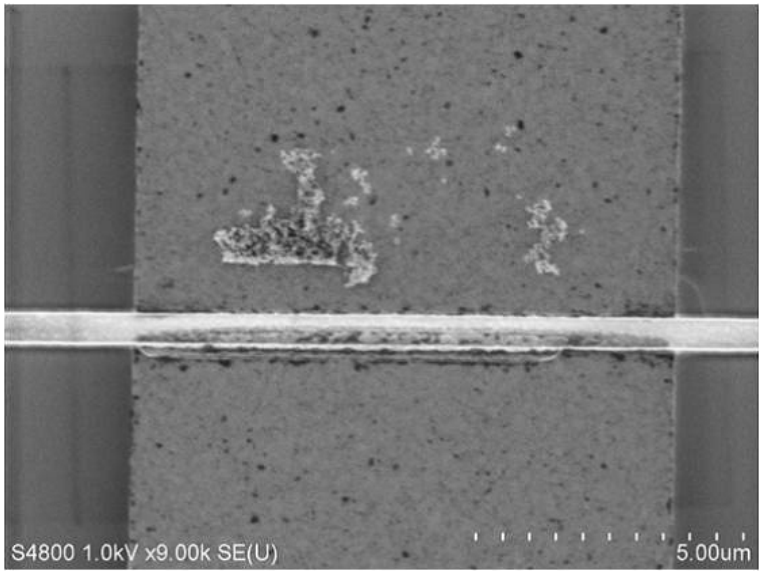

Fig. 3.1.5: SEM image of the fabricated device after CVD growth.

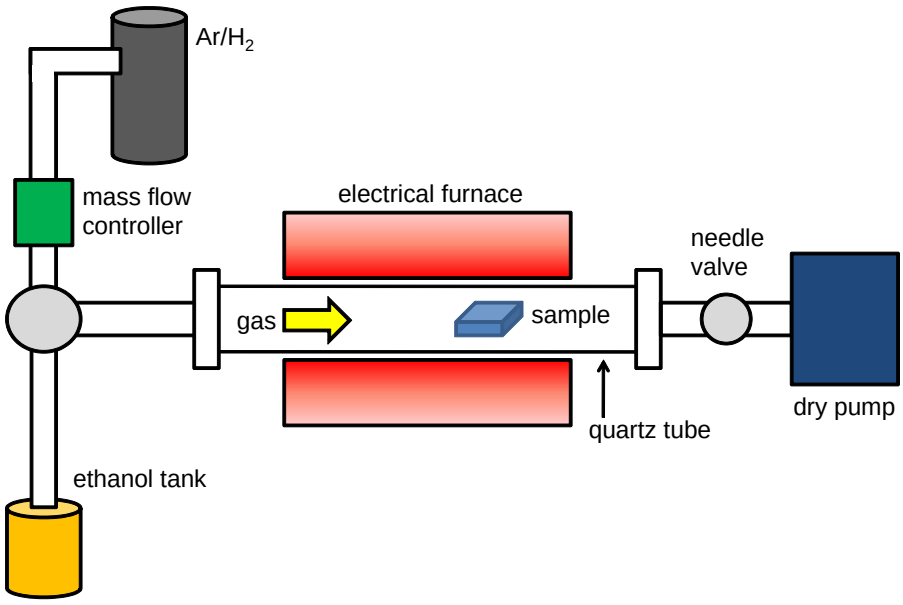

Fig. 3.1.6: A schematic of CVD system. Adapted from [26]

terminated by stopping the ethanol supply and pumping out the tube. The electrical furnace was turned off and the tube was cooled down with 50 sccm of Ar/H_2 gas flow. The chip was brought out of the tube about 10 minutes later. Fig. 3.1.4 and 3.1.5 show optical and SEM images of the fabricated device after CVD process respectively. In Fig. 3.1.5, there are catalyst particles supported on the silica on the electrode.

3.2 Electrical measurements of devices

In order to examine whether SWCNTs are suspended over trenches, electrical characteristics of devices were measured. Yield of devices were also investigated for obtaining semiconducting individual SWCNT FETs.

3.2.1 Characteristic features of fabricated individual single-walled carbon nanotube field effect transistors

At first, for confirmation of conduction, gate voltage was changed from -8 V to 8 V and from 8 V to -8 V at steps of 2 V while the voltage between source and drain was fixed at 0.1 V. If the resistance between source and drain is smaller than 5.0×10^{-7} Ω, gate and drain dependences are measured in detail.

Fig. 3.2.1 and 3.2.2 shows typical characteristics of drain current to gate and drain voltage in semiconducting and metallic SWCNTs. The characteristic features of CNT FETs are explained by Schottky barrier model[44][45][46]. Schottky barrier between metal and the SWCNT becomes thiner applying gate voltage, leading to the increase of tunneling current. In semiconducting SWCNTs, drain current was observed in the area of negative gate voltage. This is because oxygen molecules adsorbing onto the surface of SWCNTs work as acceptors[46]. Therefore, as-grown SWCNTs display p-type semiconductors. In the negative region, holes are injected into the SWCNT as shown in Fig. 3.2.3 left. In the positive bias, However, electrons can not tunnel because of higher Schottky barrier compared with holes. In contrast, drain current in metallic SWCNTs was observed in both negative and positive bias since the band gap of metallic SWCNTs is very small (a few meV). Negative differential conductance due to electron-phonon scattering by optical phonons[47][48] was also observed in metallic SWCNTs. In both semiconductor and metallic devices, hysteresis was observed due to charge traps by adsorption of water molecules[49]. Amount of drain current in fabricated devices is between 10^{-9} and 10^{-7} A in semiconducting SWCNTs, and between 10^{-7} and 10^{-5} in metallic SWCNTs. Amount of current is mainly dominated by contact resistance between SWCNTs and elec-

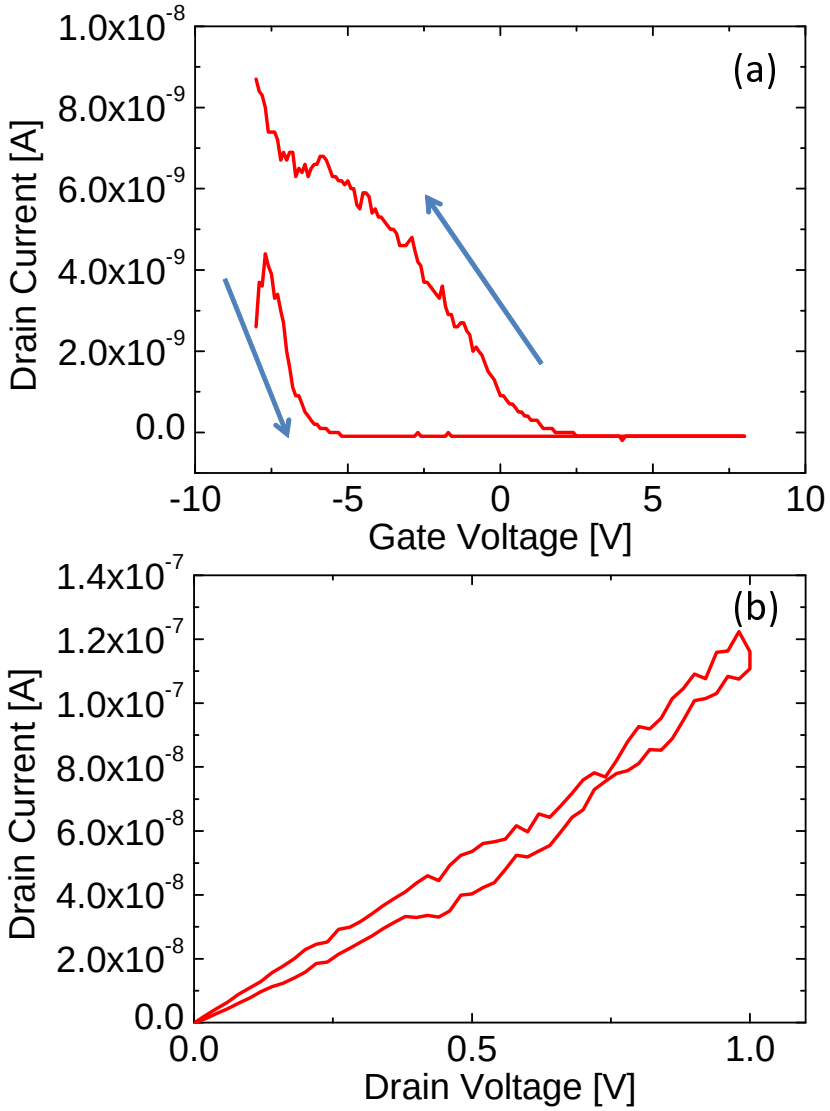

Fig. 3.2.1: (a) Gate characteristic feature in the semiconducting SWCNT FET. Drain voltage is fixed to be 0.1 V. (b) Drain voltage dependence of the drain current. Gate voltage is fixed to be -8 V.

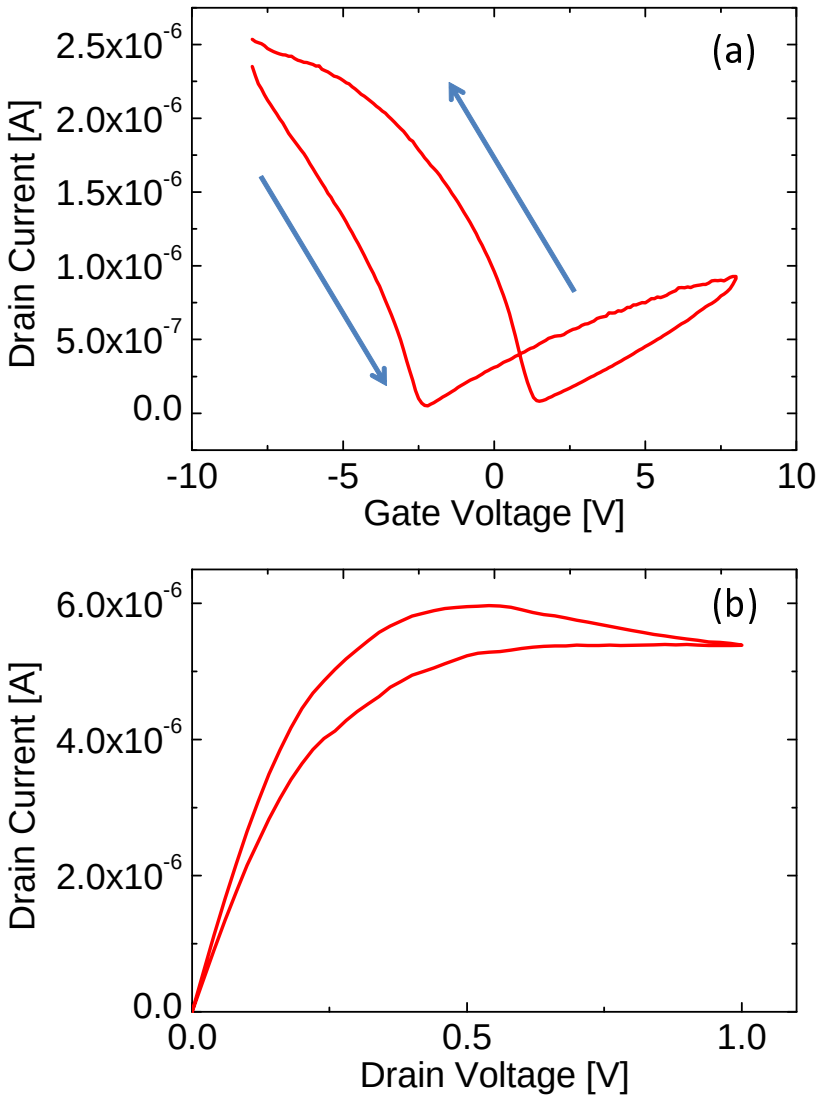

Fig. 3.2.2: (a) Gate characteristic feature in the metallic SWCNT FET. Gate voltage is -8 V. (b) Drain voltage dependence of the drain current. Gate voltage is fixed to be -8 V.

trodes. In conclusion, it is confirmed that good quality semiconducting SWCNT FETs could be fabricated.

3.2.2 Yield of individual single-walled carbon nanotube field effect transistors

In order to obtain a lot of individual SWCNT FETs, yield of devices needs to be controlled. Electrical properties of 96 devices as shown in Fig. 3.2.4 were measured, and the yield was calculated. The between 10 % and 20% is though to be better for individual SWCNT devices. If the rate of devices are too large, a number of SWCNTs or bundles are suspended over trenches.

Fig. 3.2.5 and 3.2.6 shows chip maps of devices which were grown in different catalyst conditions. The sample in Fig. 3.2.5 is grown with 12 mg of Co and 200 mg of silica, and the sample in Fig. 3.2.6 is grown with 6 mg of Co and 100 mg of silica. Green regions in the chip maps indicate devices operating as semiconducting or metallic SWCNT FETs. Red regions and white regions denote devices which show anomalous properties, such as gate leaking, and no current respectively. The yield of the sample in Fig. 3.2.5 are about 33.3%. The value is a little too large. There are also a lot of gate leaking devices because of large number of SWCNTs. The yield of the sample in Fig. 3.2.6 is about 19.8%, and this is a good rate. Number of gate leaking devices are fewer compared with the sample in Fig. 3.2.6. A chip map of the sample grown with 40 mg Fe and 200 mg silica is also shown in Fig. 3.2.7. It is found that number of grown SWCNTs are much fewer than that grown with Co catalyst. Moreover semiconducting SWCNT FETs tend to increase compared with the Co catalyst sample. This is attributed to fewer bundles of SWCNTs. The condition of Fe catalyst needs to be more improved. To conclude, Co catalyst with 100 mg silica is better. Finally, the condition of CVD system must to be taken into account.

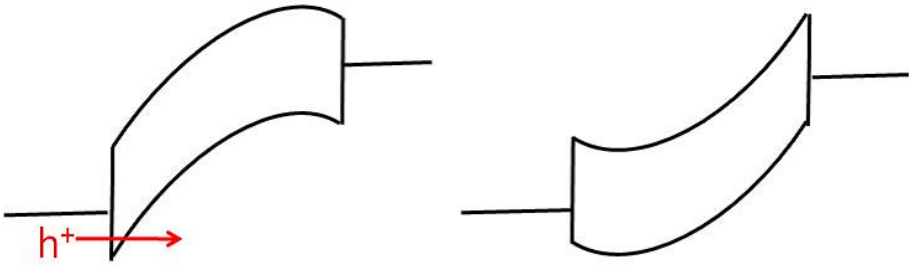

Fig. 3.2.3: Schematics of band structure of semiconducting SWCNT FETs in the negative bias (left) and the positive bias (right).

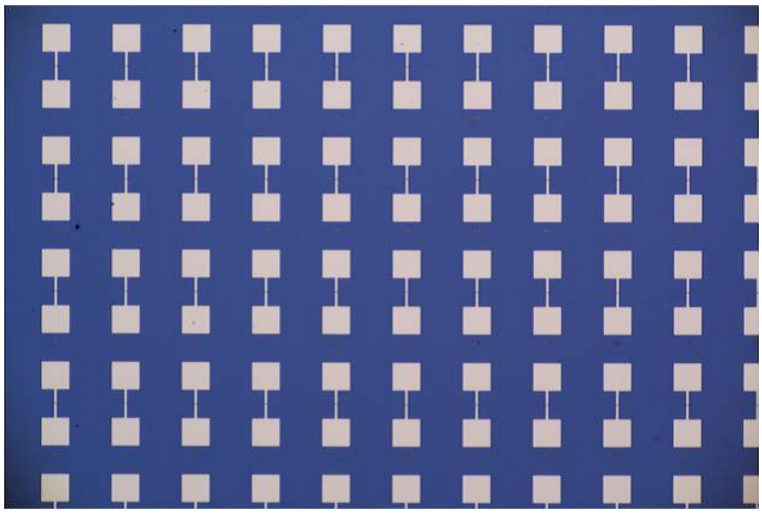

Fig. 3.2.4: An optical image of array of devices

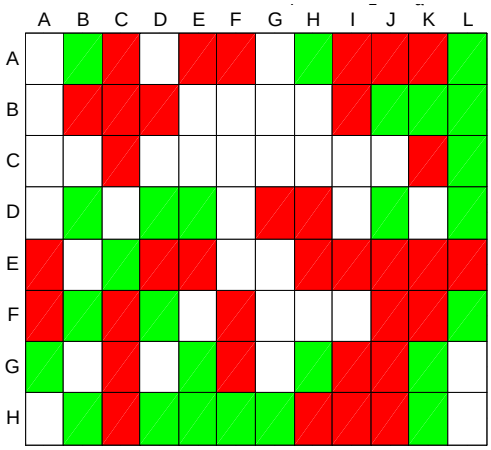

Fig. 3.2.5: Chip map in the SWCNT FETs grown with 200 mg of silica and 12 mg of Co.

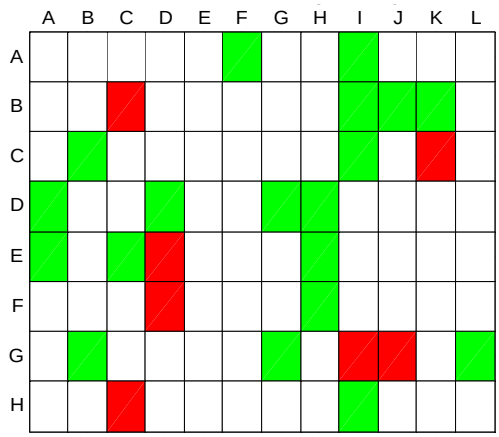

Fig. 3.2.6: Chip map in the SWCNT FETs grown with 100 mg of silica and 6 mg of Co.

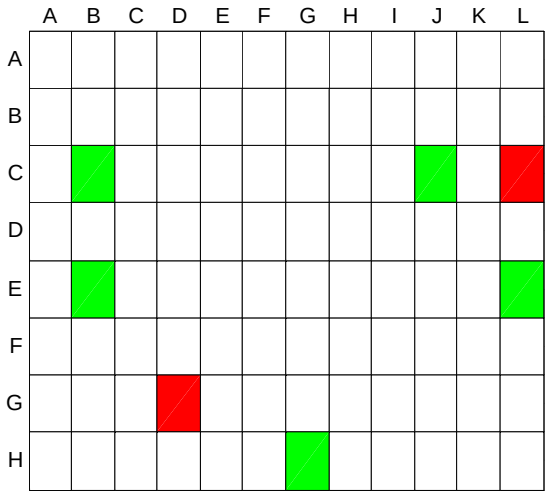

Fig. 3.2.7: Chip map in the devices grown with 200 mg of silica and 40 mg of Fe.

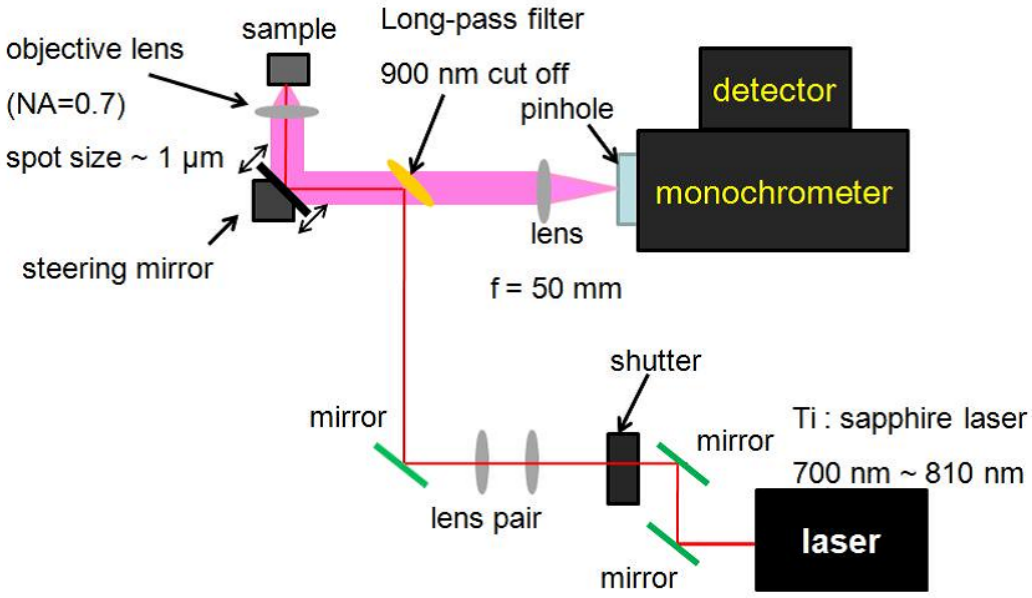

Fig. 3.2.8: A schematic of PL measurement system. Taken from [26]

3.3 Optical measurements of single-walled carbon nanotubes

In devices which displayed the features of semiconducting SWCNTs, PL spectroscopy was performed to observed light emission. Moreover, in order to identify the chirality of the SWCNT and confirm that the SWCNT is individual, PL excitation (PLE) measurement was conducted. Fig. 3.2.8 shows an optical measurement system. A wavelength tunable continuous wave Ti:sapphire laser (700 to 825 nm) is used as a light source for excitation of the sample, and the laser beam is focused with a miroscope objective (Mitutoyo, Mplan Apo NIR-HIR, 100×, NA 0.7). The excitation power is varied using a set of neutral density (ND) filters. PL signal from samples is collected with the same objective, transmitted through a dichroic filter and dispersed by a grating monochromator (Acton SP2300i, 150ng/mm, blazed at 1.25 μm) onto a liquid nitrogen cooled InGaAs photodiode array (Acton, OMA-V 512) to obtain PL spectra. In order to subtract the background signal, a shutter is used. Samples are mounted on a three-axis ball bearing linear stage for rough scanning of the samples. A voltage-controlled fast steering mirror (Optics In Motion LLC.) is placed before the objective lens in order to precisely control the position of the laser spot on the samples and acquire two-dimensional PL images.

3.3.1 Photoluminescence imaging

Firstly, the laser spot was moved near the trench of the device by driving the linear stage. Then, PL images around the trench were taken in order to make sure whether PL from the SWCNT was observed.

Fig. 3.3.1 shows a schematic and PL images around the trench of the device respectively. After the linear stage is fixed, the laser spot was scanned (200 nm step) utilizing the steering mirror and, in parallel, PL spectrum was collected at each position. White arrows in the schematic image indicate the scan direction. All the spectra were taken with 750 nm excitation wavelength, 0.35 mW laser power, and 500 ms accumulation time. By extracting the emission intensities around 1130 nm and 1393 nm from all of the acquired PL spectra and re-potting it two dimensionally, PL images at 1130 nm and 1393 nm were obtained. The PL image at 1130 nm shows the distribution of PL intensity from the silicon substrate, indicating the position of a trench and electrodes. Since position of trench in PL image at 1130 nm corresponds with that of the PL spot in 1393 nm image, this PL spot is due to luminescence from the suspended SWCNT. Fig. 3.3.2 shows PL spectra from silicon substrate and the SWCNT in the trench. A narrow peak severalfold stronger than PL from silicon was observed from the SWCNT. It can be confirmed that there is a luminescent

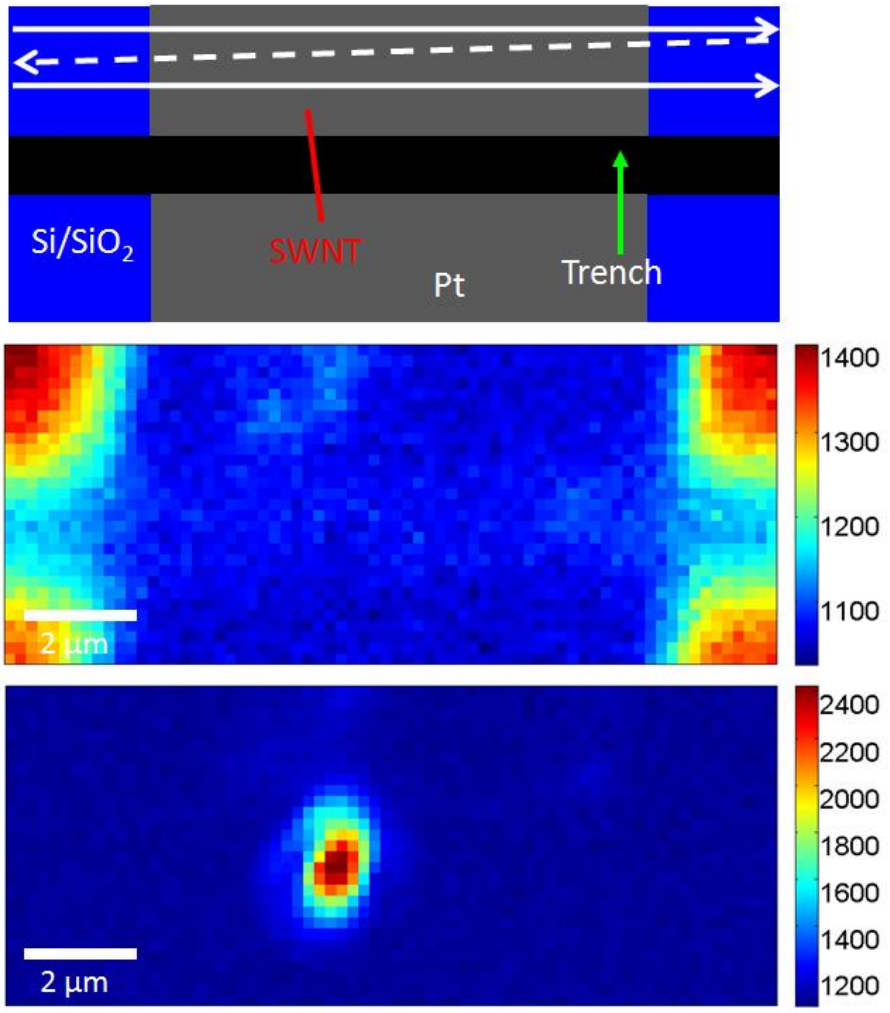

Fig. 3.3.1: A schematic and PL images around the trench. PL images are obtained by extracting and re-plotting PL intensities at 1130 nm and 1393 nm. A bright region in a PL image of 1393 nm is thought to be PL from a suspended SWCNT

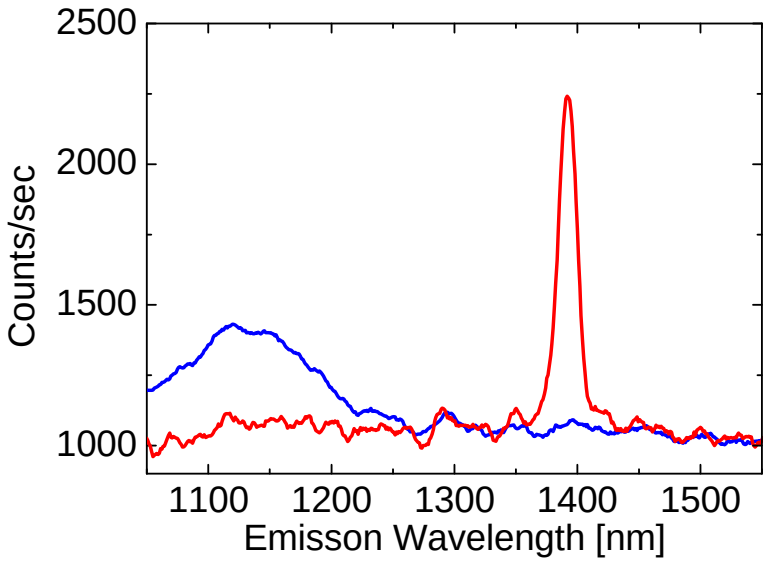

Fig. 3.3.2: PL spectra from silicon substrate (blue) and the SWCNT at the trench (red) respectively.

suspended SWCNT in the device. However, we have no idea whether this SWCNT is an individual tube or bundles.

3.3.2 Photoluminescence excitation map

In order to assign a chiral index of the SWCNT, a PL excitation (PLE) map was acquired and value of E_{11} and E_{22} energies were extracted. The steering mirror was moved to the position of the SWCNT obtained in Fig. 3.3.1. PL spectra were measured changing excitation wavelength within the range from 710 nm to 820 nm (2-3 nm step). Fig. 3.3.3 shows two dimensional plot of PL intensity as a function of emission wavelength and excitation wavelength, which is called PLE map. Light emission at the wavelength of 1393 nm was observed and this PL is enhanced around the excitation wavelength of 800 nm. This SWCNT sample is thought to be individual, because there is only a single peak in the map. Fig. 3.3.4 indicates excitation wavelength dependence of PL intensity at the emission wavelength of 1393 nm. From this figure, the value of E_{22} can be measured. E_{11} and E_{22} energies were measured to be 0.892 eV and 1.56 eV, respectively. This individual SWCNT can be assigned to be (9,8)[18].

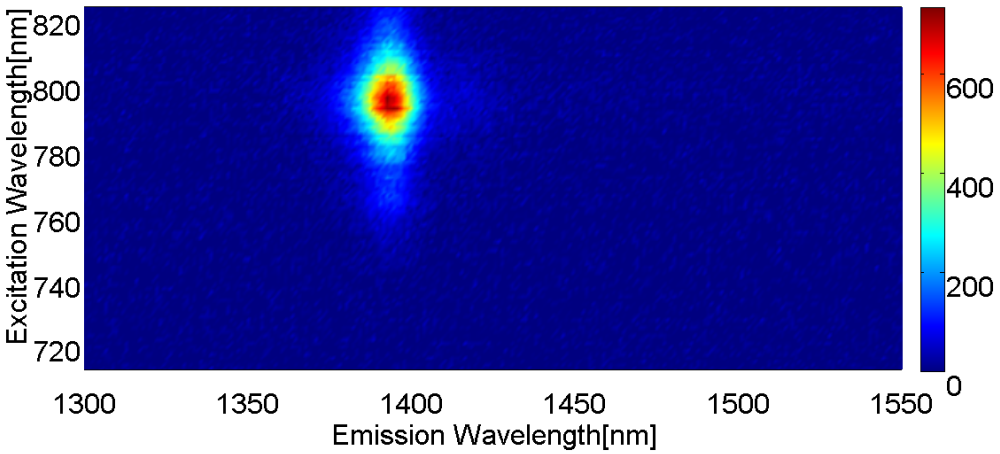

Fig. 3.3.3: A PLE map for the SWCNT.

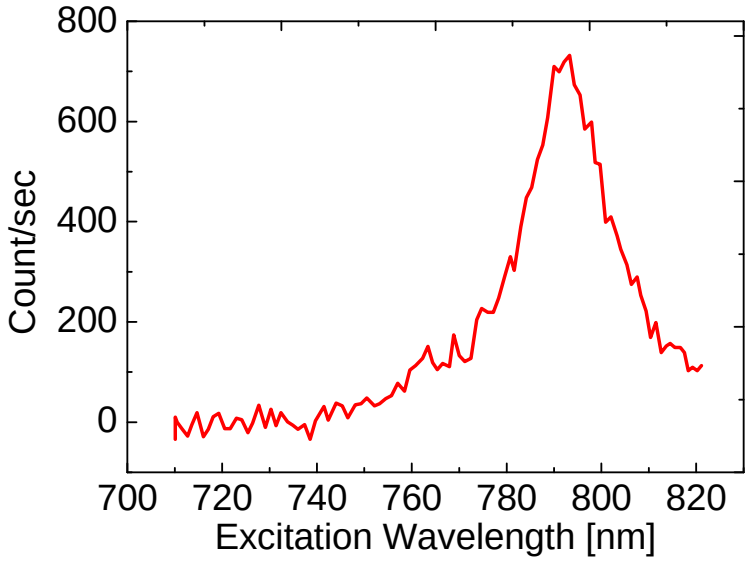

Fig. 3.3.4: Cross section of the PLE map at emission wavelength of 1393 nm.

Chapter 4 Electric field effect on photoluminescence from single-walled carbon nanotubes

4.1 Gate dependence of photoluminescence

4.1.1 The result of gate voltage dependence

First of all, PL from individual SWCNT whose chirality was identified was measured while the gate voltage was changed without the drain bias. Fig. 4.1.1 shows two dimensional plot of PL from a (10,6) SWCNT as a function of wavelength and the gate voltage. The gage voltage was changed from -2 V to 2 V in this sample. PL around 1330 nm was observed, and the intensity drastically decreased as the gate voltage went up. PL quenching was observed at both negative and positive biases. On the other hand, the emission wavelength does not seem to be shifted in Fig. 4.1.1.

For more detailed analysis, each PL spectrum was fitted by the Lorentz function as shown in Fig. 4.1.2.

$$y = A\frac{w^2}{(x - x_0)^2 + w^2} + y_0 \tag{4.1.1}$$

From the fit by Eq. 4.1.1, the center wavelength ($= x_0$) and PL intensity ($\propto Aw$) were extracted. Fig. 4.1.3, 4.1.4 and 4.1.5 show results of various measurements in several SWCNT FETs. (a), (b) and (c) in each figure denote a gate dependence of drain current, a PLE map and a gate voltage dependence of PL intensity (red) and emission wavelength (blue) extracted by using Eq. 4.1.1.

It is clear that emission wavelength is slightly blue shifted at a few nm in all the devices as the gate voltage is applied. This is not caused by the screening of Coulomb interaction by carriers since emission photon energy must be red shifted, due to the screening effect. Moreover, this energy shifts are 2∼7 meV and too smaller compared with reported values in the screening effect (∼30 meV)[18]. Therefore, origin of the blue shift needs to be considered.

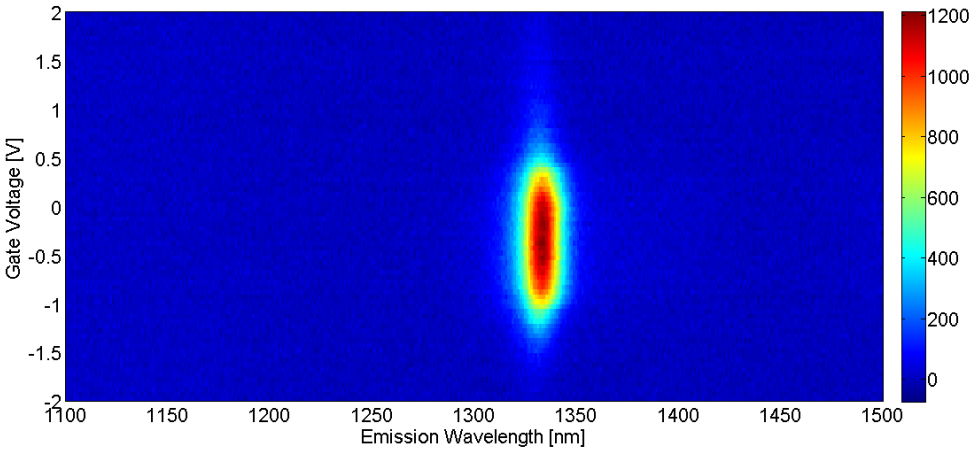

Fig. 4.1.1: Two dimensional plot of PL intensity as a function of emission wavelength and gate voltage.

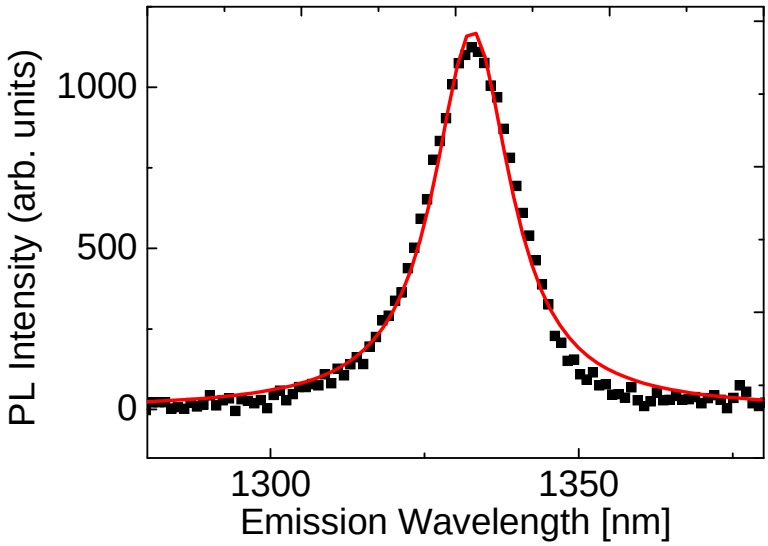

Fig. 4.1.2: An example of a PL spectrum fitted by Lorentz function.

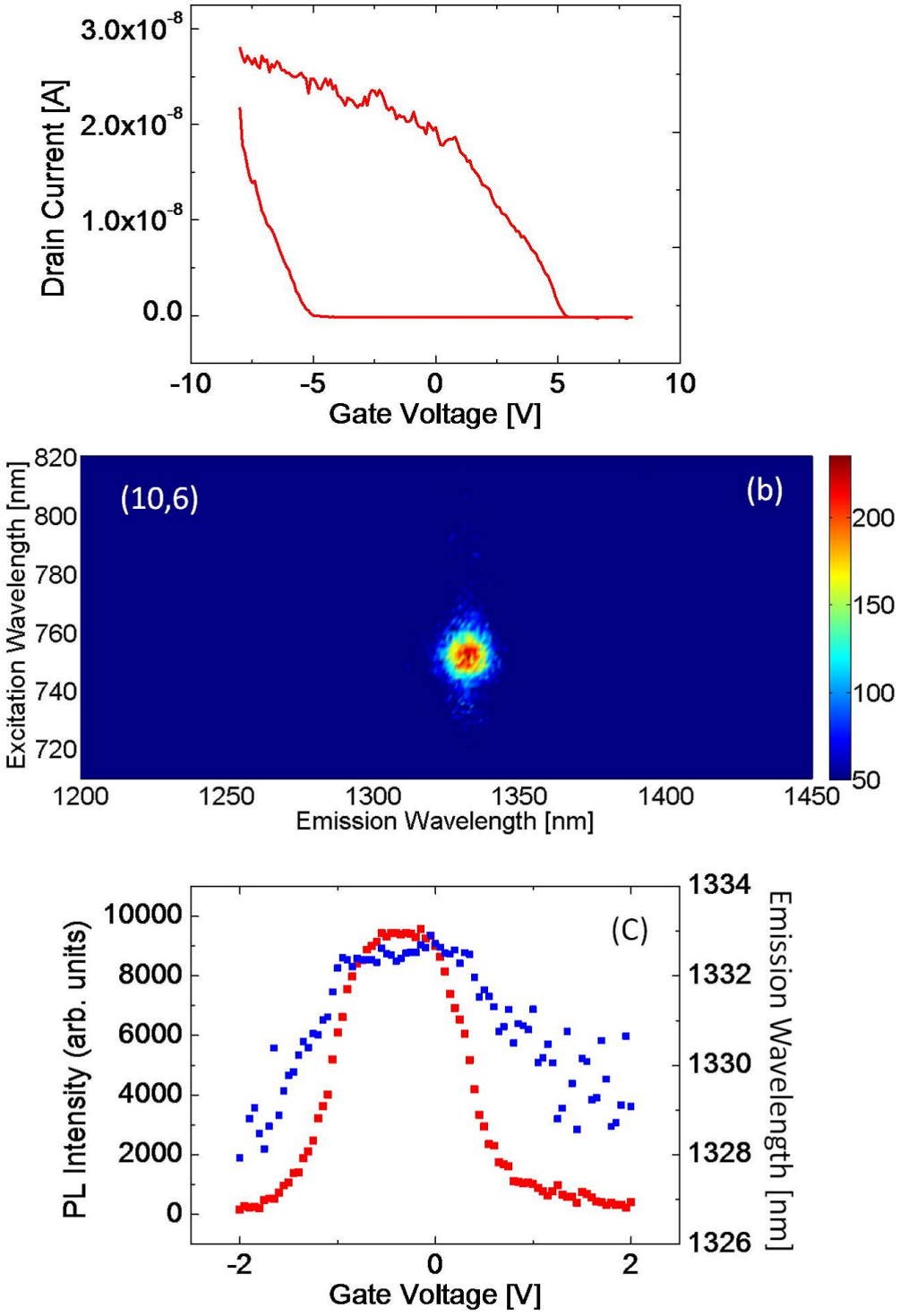

Fig. 4.1.3: Results of various measurements of a (10,6) SWCNT FET. (a) Gate characteristics of Drain current. (b) A PLE map. (c) Gate voltage dependences of PL intensity (red) and emission wavelength (blue).

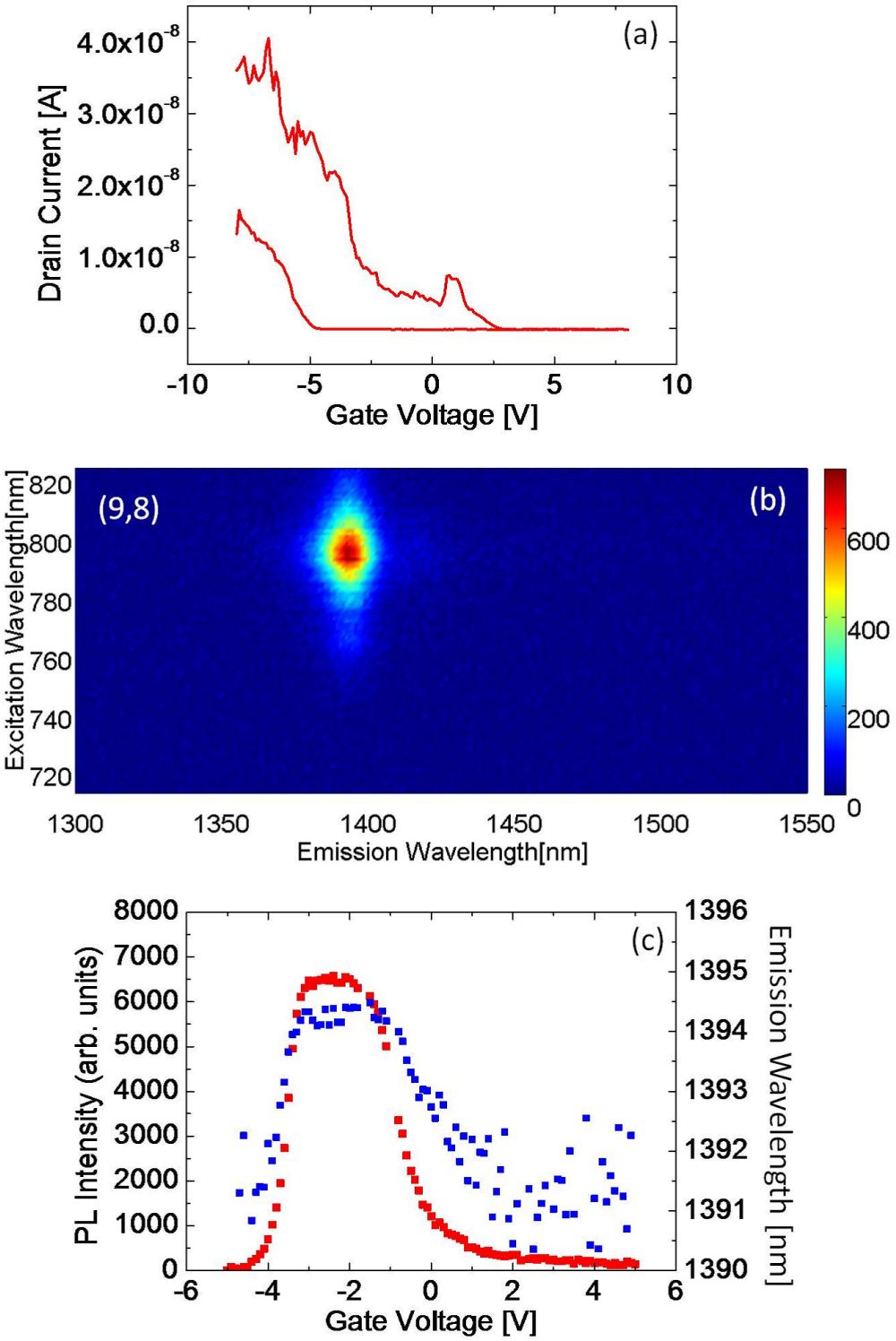

Fig. 4.1.4: Results of various measurements of a (9,8) SWCNT FET. (a) Gate characteristics of Drain current. (b) A PLE map. (c) Gate voltage dependences of PL intensity (red) and emission wavelength (blue).

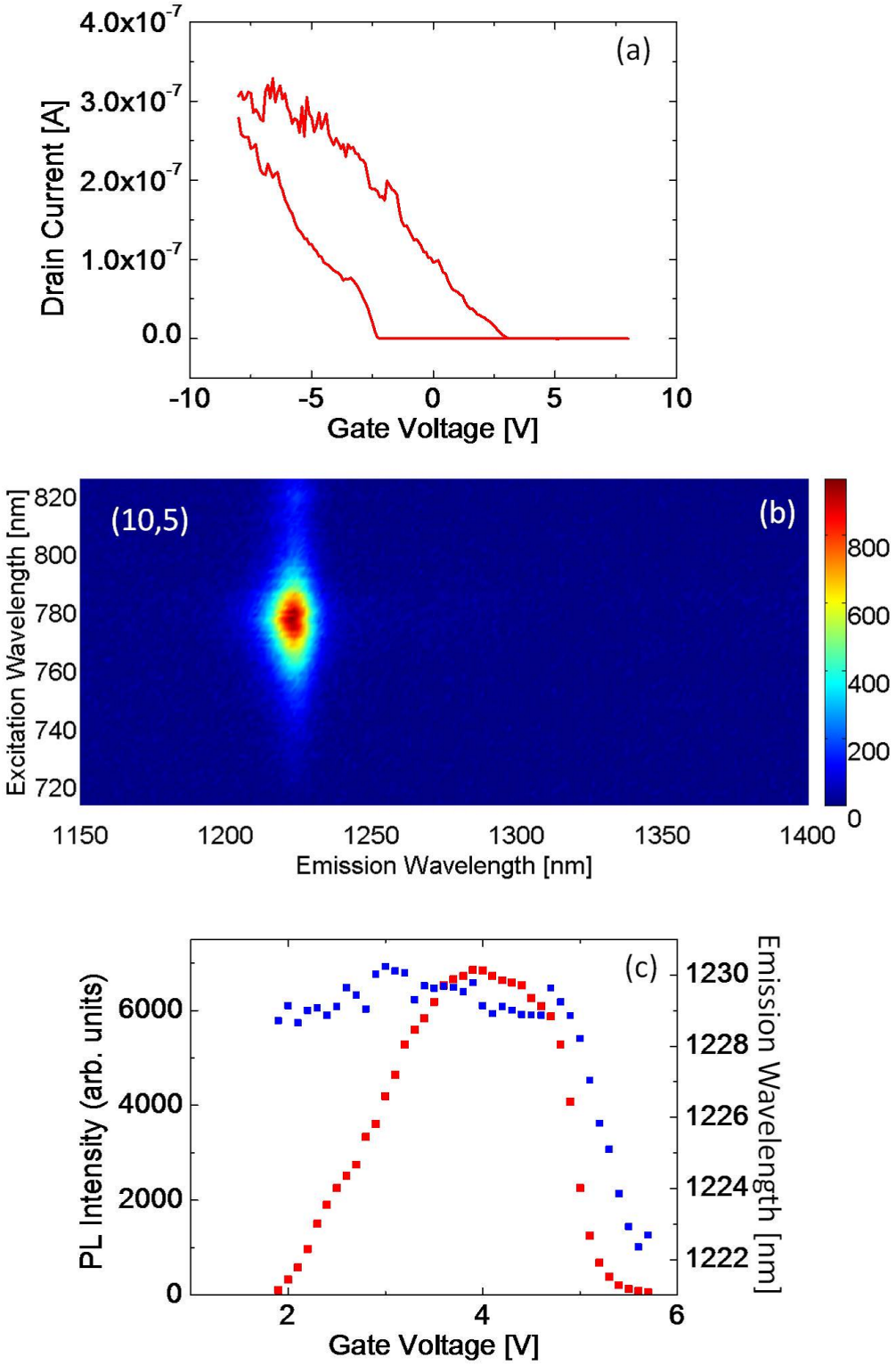

Fig. 4.1.5: Results of various measurements of a (10,5) SWCNT FET. (a) Gate characteristics of Drain current. (b) A PLE map. (c) Gate voltage dependences of PL intensity (red) and emission wavelength (blue).

4.1.2 Origin of the blue-shift in electric field

There are several possible reasons for the blue shift of PL from a SWCNT in the electric field. Strain of the SWCNTs or molecule desorption are considered.

Firstly, Strain effect is assumed. When the gate voltage is applied, a suspended SWCNT is pulled by Coulomb attractive force, leading to addition of uniaxial strain. It was reported that the band gap of SWCNTs is changed in a case SWCNTs are strained[50]. The change of band gap is different between type 1 ($n - m \equiv 1$) and type 2 ($n - m \equiv 2$) SWCNTs given same strain. For example, when SWCNTs are deformed by uniaxial tensile strain, E_{11} energy in type 1 SWCNTs are blue shifted. In contrast, E_{11} in type 2 SWCNTs are red shifted under the tensile strain. Experimentally, both red and blue shifts in E_{11} energy is observed from deformed SWCNTs[51][52]. Decrease of PL intensity due to the deformation is also reported. The (10,6) in Fig. 4.1.3 and (9,8) SWCNT in Fig. 4.1.4 belong in the type 1 SWCNTs, and the (10,5) in Fig. 4.1.5 belong in the type 2 SWCNTs. However, Emission Wavelengths are blue shifted in all the devices. This fact indicates that the energy shifts are caused due to the strain effect.

Then, gas desorption is considered. It is reported that energy shift is caused by molecules such as water or oxygen adsorbing on the surface of trench-suspended SWCNTs.[43]. Therefore it is possible that blue shift occurs by migration of polar molecules like water by electric field. Fig. 4.1.6 shows the relation between PL intensity and emission wavelength. Emission wavelength is uncorrelated to PL intensity, indicating that the energy shift of emission wavelength is independent of PL quenching by applying gate voltage. This fact supports the gas desorption. However, more investigations are also needed to confirm the effect of migration of molecules.

4.1.3 Simulation of PL quenching

It is reported that there are two possible reasons for PL quenching[20][53]. One is phase space filling, and the other is an increase of scattering with excitons by carrier doping called phonon assisted indirect exciton ionization process (PAIEI)[54][55]. Fig. 4.1.7 and 4.1.8 show schematics of PAIEI and phase space filling respectively. In PAIEI process, The exciton decays by emission of a phonon, creating an intraband electron-hole pair that satisfies nergy and momentum conservation. Fig. 4.1.7 indicates a condition where electrons are doped, and the same phenomenon occurs in hole-doped the valence band. In contrast, in phase space filling, PL quenching is caused since occupied states in the conduction band (unoccupied states in the valence band) cannot contribute to generating excitons. In order to evaluate which effects are dominant in the field-induced SWCNTs, experimental data is compared with simulation.

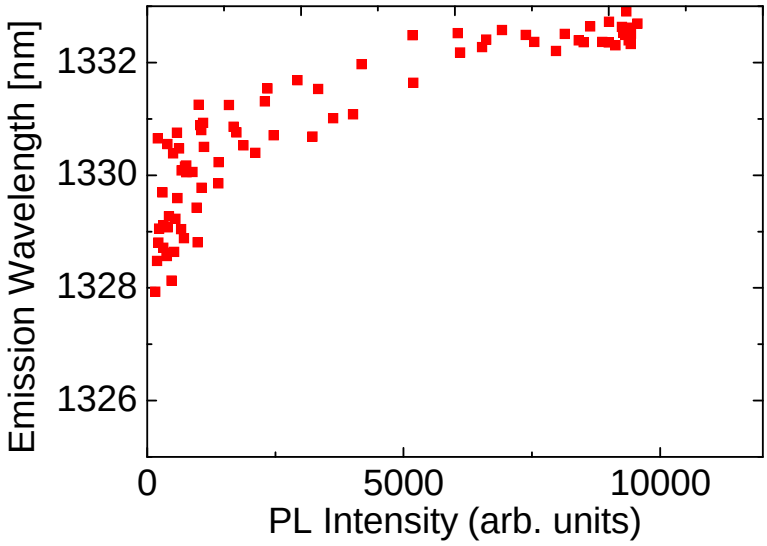

Fig. 4.1.6: Relations between PL intensity and emission wavelength.

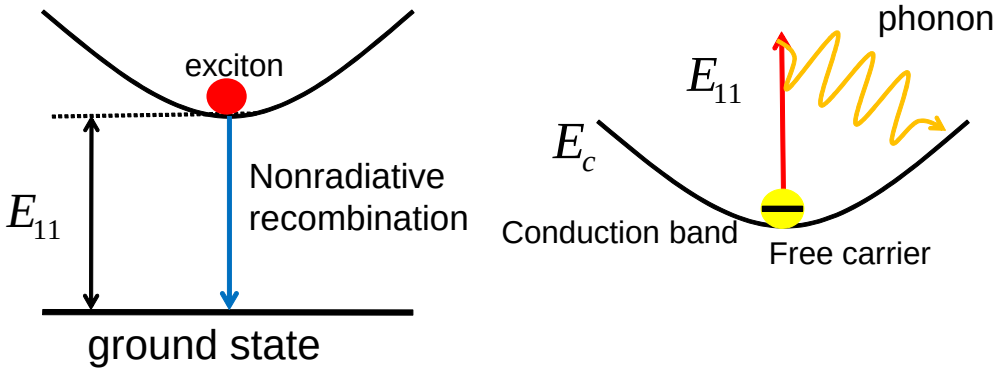

Fig. 4.1.7: A schematic of phonon-assisted indirect exciton ionization process (PAIEI).

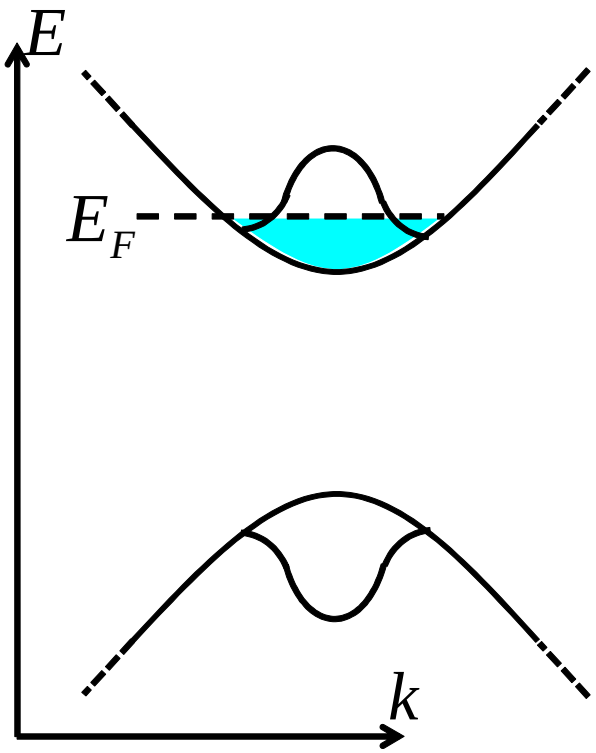

Fig. 4.1.8: A schematic of phase space filling.

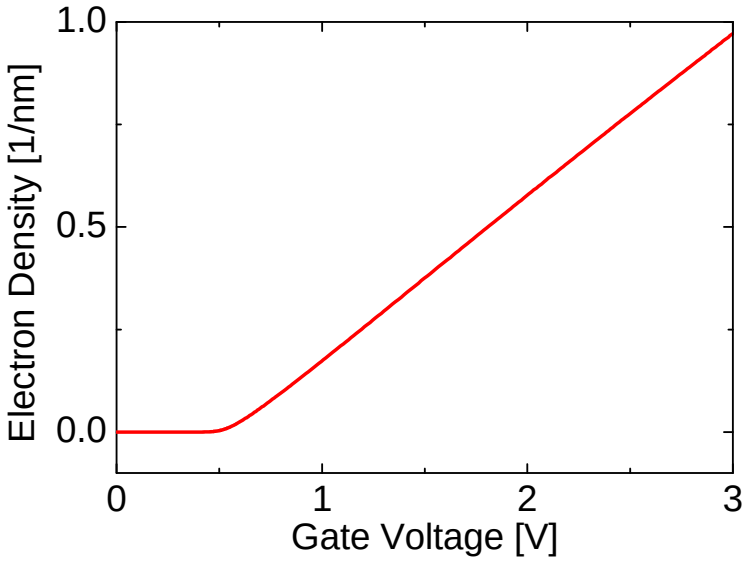

Fig. 4.1.9: Gate voltage dependence of Doped electron density. (Gate capacitance $C_g = 0.07$ pF/cm)

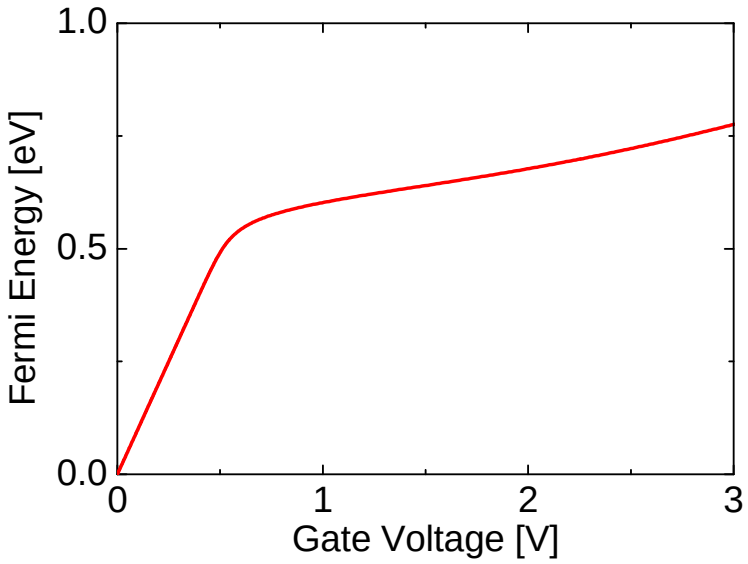

Fig. 4.1.10: The calculated Fermi energy as a function of gate voltage. (Gate capacitance $C_g = 0.07$ pF/cm)

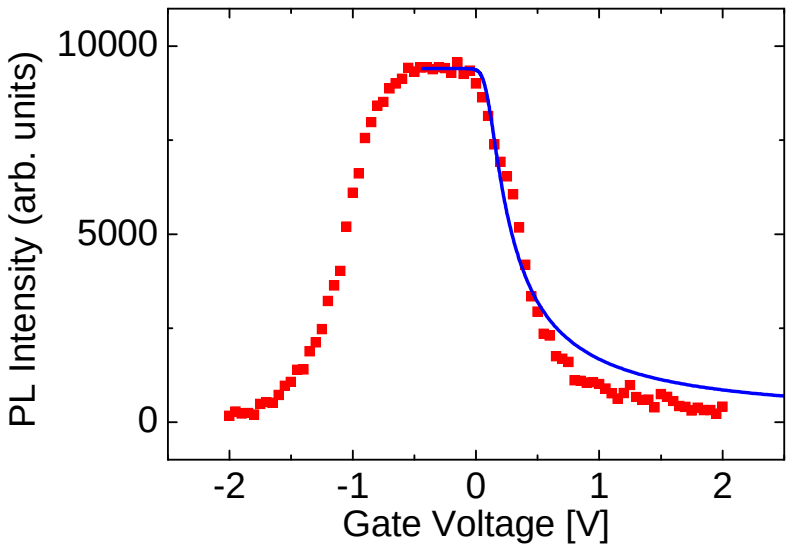

Fig. 4.1.11: A result of theoretical calculation assuming PAIEI model fitted to the experimental data in Fig. 4.1.3(c). $C_g = 0.7$ pF/cm, $r_0 = 2.0$ nm

Simulation assuming phonon assisted indirect exciton ionization

Firstly, PAIEI process is assumed. A relation between Fermi energy E_F and gate voltage V_g is written as follow.

$$V_g = \frac{E_F}{e} + \frac{e\rho}{C_g}, \tag{4.1.2}$$

where e is an electron charge, and C_g is the gate capacitance. Doped electron density ρ is defined by[56]

$$\rho = \int_{\Delta}^{\infty} f(E) \frac{4}{\pi \hbar v_f} \frac{E}{\sqrt{E^2 - \Delta^2}} dE, \tag{4.1.3}$$

$$f(E) = \frac{1}{1 + \exp\left(\dfrac{E - E_F}{k_B T}\right)}, \tag{4.1.4}$$

where $\hbar$ is the reduced Planc's constant, k_B is the Boltzman canstant, T is the absolute temperature, $f(E)$ is Fermi Dirac distribution function and $v_f = 8 \times 10^5$ ms^{-1} is the Fermi velocity. Half the many-body band gap Δ is obtained using following equation[37]

$$\Delta = \frac{1}{2}\left(\frac{0.34 \text{ eV}}{d_t} + \frac{1.11 \text{ eV}}{d_t + 0.11}\right), \tag{4.1.5}$$

where the nanotube diameter d_t is in nm. Fig.4.1.9 and 4.1.10 show calculated electron density ρ and Fermi energy E_F as a function of gate voltage. C_g is assumed 0.7 pF/cm ,compared with [20]. Fermi energy is saturated at high gate voltage, and electron density is proportional to gate voltage 0.5 V.

The nonradiative decay rate in the PAIEI process at an electron density ρ is described as

$$\Gamma_e = \frac{2\pi}{\hbar} \frac{a S_1 \hbar^2 \omega^2}{2\pi C d} \frac{k_e r_0}{(1 + k_e^2 r_0^2)^{2.6}} \frac{\rho}{E_e}, \tag{4.1.6}$$

where d is the tube diameter, $\hbar\omega$ is the G-mode phonon energy, $S_1 = 2.5$ is an effective interband Huang-Rhys factor, $C \approx 0.65$ is the wave function normalization constant and $a = 5.39$ Å^2[55]. E_e and k_e indicates a energy and a wave number of the excited electron, respectively, represented as

$$E_e = \Delta + E_{11} - \hbar\omega, \tag{4.1.7}$$

$$k_e = \frac{\sqrt{E_e^2 - \Delta^2}}{\hbar v_f}, \tag{4.1.8}$$

where E_{11} is emission energy of SWCNTs. It is noted that decay rate in the PAIEI Γ is proportional to carrier density ρ. The excitonic radius r_0 is theoretically reported

to be 1$\sim$ 2 nm[57]. r_0 in (10,6) SWCNTs is assumed to be 2 nm. PL intensity I_{PAIEI} is proportional to following expression

$$I_{PAIEI} \propto \frac{\tau_r^{-1}}{\tau_r^{-1} + \tau_{nr}^{-1} + \Gamma_e(\rho)} \tag{4.1.9}$$

where τ_r and τ_{nr} is radiative and nonradiative life time respectively. There are several theoretical and experimental reports about values of τ_r and τ_{nr}[58][59][60][15]. From these reports, τ_r and τ_{nr} is determined to be 10 ns and 100 ps respectively. Fig.4.1.11 shows the result of simulation with $C_g = 0.7$ pF/cm and $r_0 = 2.0$ nm. The theoretical calculation is in good agreement with the experimental data. A little deviation is attributed to the parameter in Eq.4.1.6. The calculation is also done using r_0 as a fitting parameter as shown in Fig.4.1.12. PL intensity decreases more sharply as r_0 becomes smaller. Theoretical result can be fitted with experiment by changing r_0 which controls Eq.4.1.6. In conclusion, the PAIEI model can explain well PL quenching by electric field.

Theoretical calculation using phase space filling model

The distribution of electrons $f_e(k)$ which contribute to generating excitons can be written as

$$f_e(k) \propto \left|\tilde{\Psi}_{exc}(k)\right|^2, \tag{4.1.10}$$

where $\tilde{\Psi}_{exc}(k)$ is the Fourier transform of the exciton relative motion orbital wave function $\Psi_{exc}(x)$[61]. The relative motion excition wave function in one dimension can be approximated by a Gaussian function[61],

$$\Psi_{exc}(x) = \exp\left(-\frac{x^2}{2r_0^2}\right), \tag{4.1.11}$$

where $r_0 = 2$ nm is exciton radius same as in PAIEI model. Therefore,

$$\tilde{\Psi}_{exc}(k) = \exp\left(-\frac{k^2 r_0^2}{2}\right). \tag{4.1.12}$$

PL intensity I_{phase} can be written as follow

$$I_{phase} \propto \frac{\int_\Delta^\infty \frac{E}{\sqrt{E^2-\Delta^2}} \exp\left(-\frac{(E^2-\Delta^2)}{2\hbar^2 v_f^2} r_0^2\right)(1-f(E))dE}{\int_\Delta^\infty \frac{E}{\sqrt{E^2-\Delta^2}} \exp\left(-\frac{(E^2-\Delta^2)}{2\hbar^2 v_f^2} r_0^2\right)dE}. \tag{4.1.13}$$

The numerator in 4.1.13 indicate the number of unoccupied states for excitions. Fig. 4.1.13 shows a calculation result in phase filling model. Gate capacitance C_g is fixed

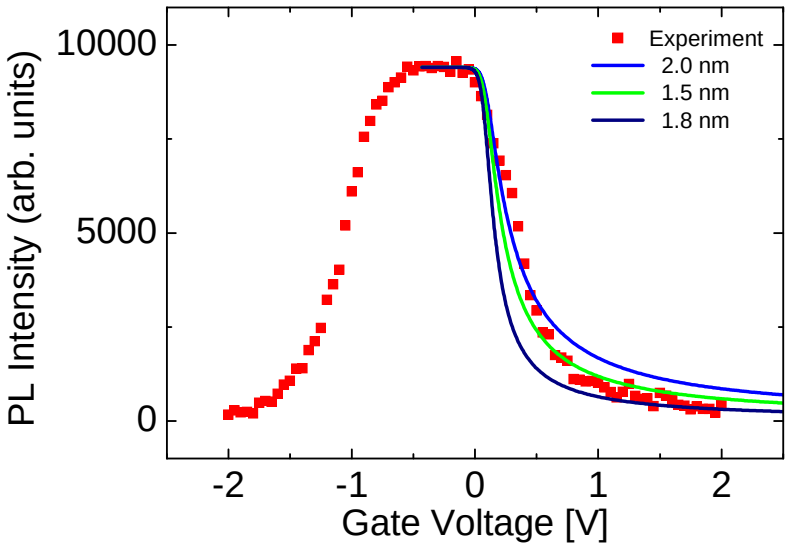

Fig. 4.1.12: The calculated PL intensity at several values of r_0 fitted to the experimental data in Fig. 4.1.3(c).

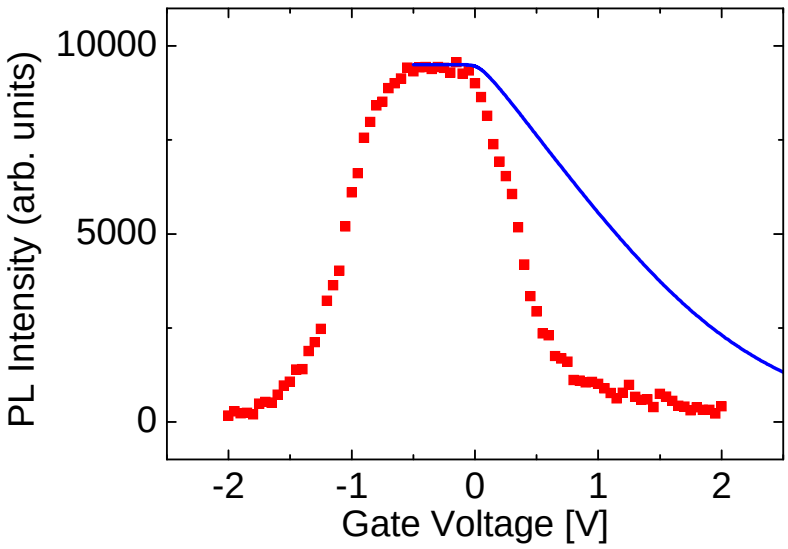

Fig. 4.1.13: Theoretical gate dependence of PL intensity using phase filling model fitted to the experimental data in Fig. 4.1.3(c).$C_g = 0.7$ pF/cm, $r_0 = 2.0$ nm

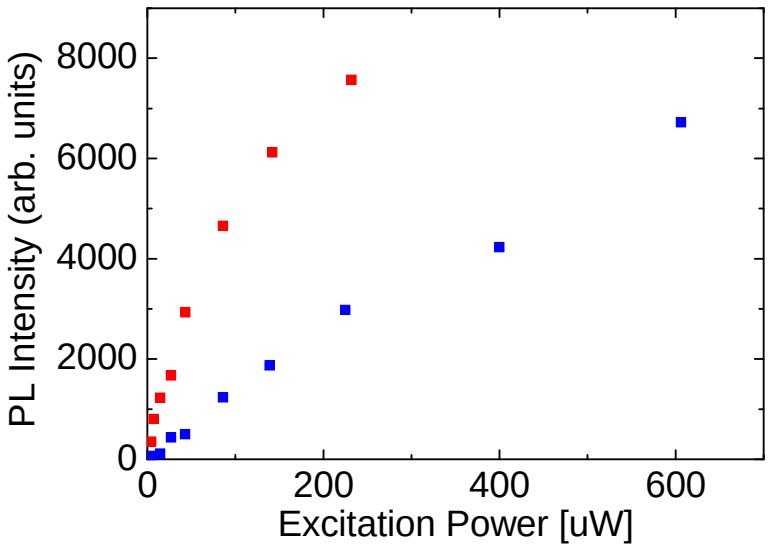

Fig. 4.1.14: Excitation power dependence of PL intensity in $V_g = 0$ V (red) and $V_g = -2$ V respectively.

to 0.7 pF/cm. The theoretical curve deviates significantly from the experimental data. Compared with PAIEI model, PL intensity is more moderately decreased. In order to fit this curve with the experimental data, larger value of C_g is needed. Therefore, phase space filling does not seem to be effective in the field-induced SWCNTs.

4.2 Excitation power dependence in the electric field

Fig. 4.1.14 shows excitation power dependence of PL intensity with and without gate bias. Without electric field, PL intensity saturates as excitation power becomes larger. This behavior is explained by the effect of exciton-exciton annihilation. This process induces rapid nonradiative recombination of excitons under high excitation regime and the nonlinear behavior of PL intensity. In contrast, PL intensity under field-induced condition is increased linearly to excitation power. This suggests that number of excitons are reduced by scattering with carriers.

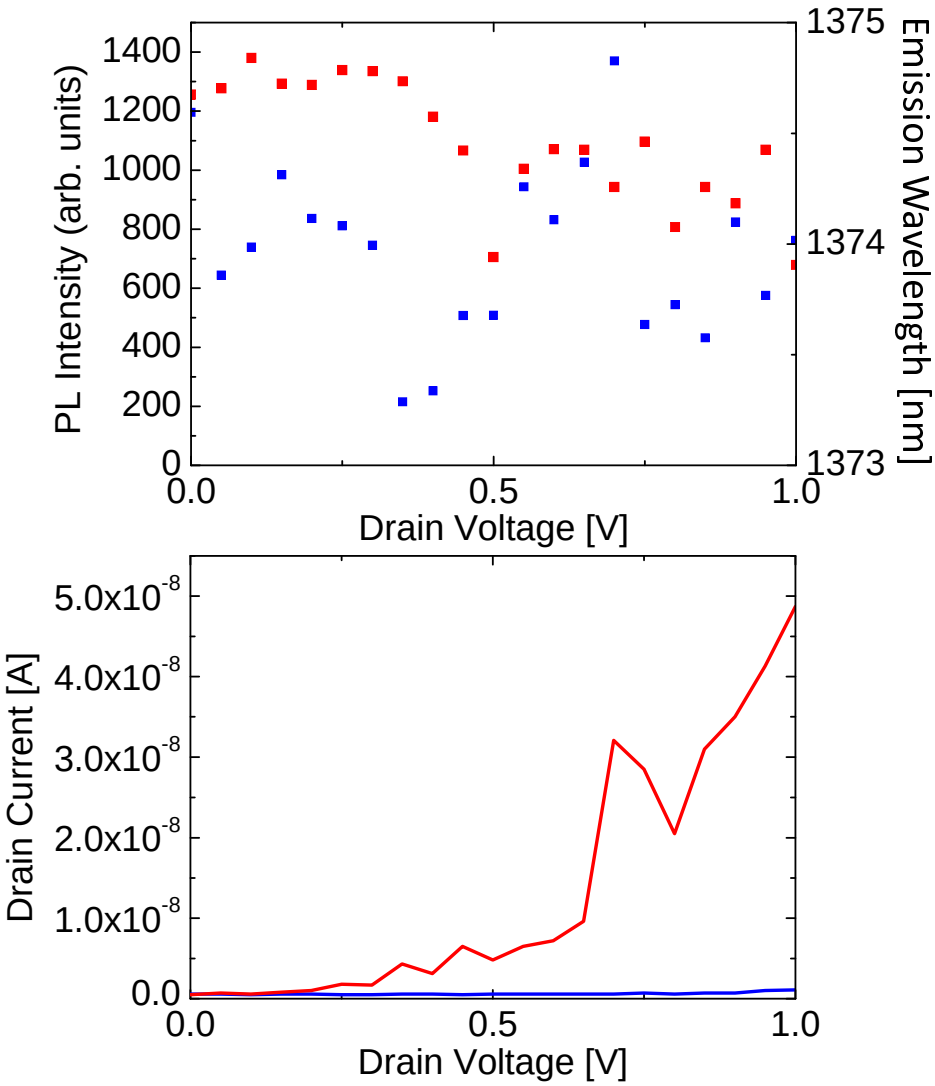

Fig. 4.2.1: Drain voltage dependence of PL intensity and emission wavelength in (9,8) SWCNT (above). Drain current as a function of drain voltage (below). The red curve is the drain current with laser excitation, the blue one is without laser.

4.3 Drain voltage dependence

Drain voltage dependence of PL was investigated as shown in Fig. 4.2.1. PL spectra were measured changing drain voltage from 0 V to 1 V and fixed gate voltage to 0 V. Emission wavelength does not seem to be shifted. A little decrease of PL intensity was observed. Compared with PL quenching in Gate bias, this change of intensity is small and moderate. This behavior seem to be different from the report in [53]. Photocurrent is observed under excitation condition while the drain current hardly flows without laser. The photocurrent is increased as the drain voltage become larger. There is not a relation between PL and the drain current. However, it is noted that the samples where the drain dependence is measured is very few. Therefore, more measurements are needed.

Chapter 5 Conclusion

Electric field dependence of PL was investigated using air-suspended individual SWCNT FETs. PL quenching and slight blue shifts are observed by applying gate voltage. The blue shifts are thought to be due to migration of polar molecules like water by electric field. Screening effect caused by doped carriers could not be observed. Compared with theoretical calculation, PL quenching is consistent with PAIEI process. Therefore, in gate-doped SWCNTs, it is suggested that PL processes is dominated by scattering with increased carriers, and screening is hardly effective.

Appendix A Device process

A.1 Effect of annealing process

After fabricating trenches, the wafer was annealed to insulate the surface of trenches in order to suppress gate leakage in devices. Without annealing, the gate leaking as shown in Fig. A.1.1 occurs in almost all devices. More than 5 μA of current flows to the gate. This gate leakage is caused by SWCNTs which contact the source electrode with gate Si as shown in Fig. A.1.2. By annealing the wafer in the presence of oxygen for 1 hour, the gate leaking device can be drastically decreased.

A.2 Condition of electron beam evaporation

A.2.1 Electron beam evaporation using ZEP520A

Since e-beam resist ZEP520A is thin, it has a low tolerance to heat, leading to hardening in e-beam evaporation process. The hardened resist can not be removed in lift off process and electrodes can not be formed. In particular, Ti can not be used for ZEP520A because too much heat is generated. Therefore, only Pt is deposited for electrodes. However, in a case of thick Pt depositon, lift off process is also failed. Moreover, without the Ti layer, electrode is easily peeled off by such as a sonication process.

A.2.2 Electron beam evaporation using OEBR CAP-112PM

OEBR CAP-112PM is thicker and more tolerant to heat than ZEP520A. By using OEBR, it becomes possible to use Ti and to deposit thicker Pt. Thanks to the Ti layer, electrodes are stable in the sonication. Therefore, it is better to use OEBR. In a case of thick or high rate depostion, however, devices displaying gate leakage as shown in Fig. A.1.1 increase. This phenomena occurs since the e-beam resist is not be removed completely. It is considered that the remaining resist exert a bad influence on devices in CVD growth. Therfore, cleaning process such as the O_2 cleaning process need to be improved.

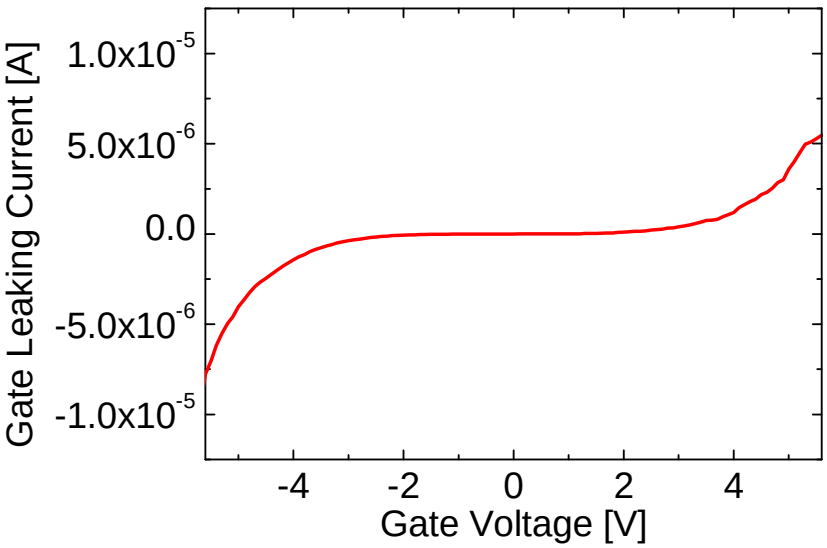

Fig. A.1.1: Typical characteristic of gate current as a function of the gate voltage in gate leaking devices

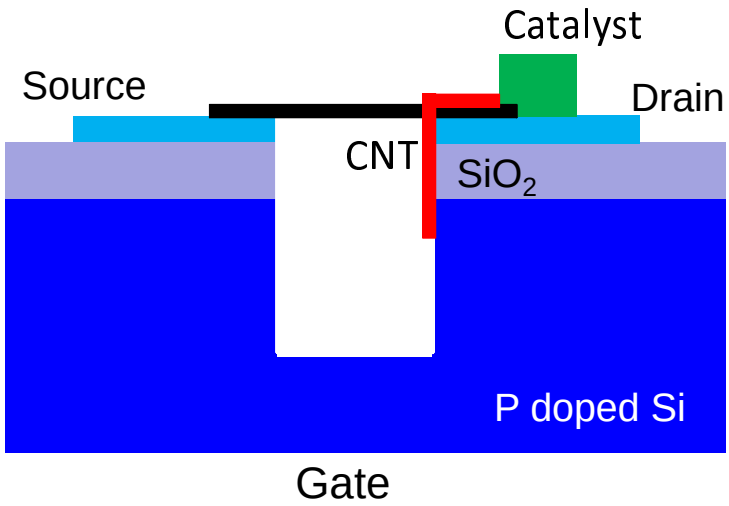

Fig. A.1.2: A schematic of gate leaking devices

Appendix B Optical measurement

B.1 Photoluminescence from bundled single-walled carbon nanotubes

PL from bundled SWCNTs is observed. A PLE map of bundled SWCNTs is shown in Fig. B.1.1. There are two resonances in the figure. This fact indicate that more than two SWCNTs are bundled. The PL quenching and the blue shifts are also observed in such the bundled SWCNTs. devices.

B.2 Hysteresis in gate voltage dependence of photoluminescence

Gate voltage dependence of PL changes with the sweeping directions of the gate voltage as shown in Fig. B.2.1 This hysteresis is attributed to charge trapping by water molecules. The gate voltage dependence is also changed with the range of the gate voltage and sweeping rate. The charge trapping makes it difficult to analyze the gate voltage dependence of PL. Therefore, PL measurements need to be conducted under an inert atmosphere such as N_2 or Ar. Alternatively, An effect of the fixed charge should be taken into account.

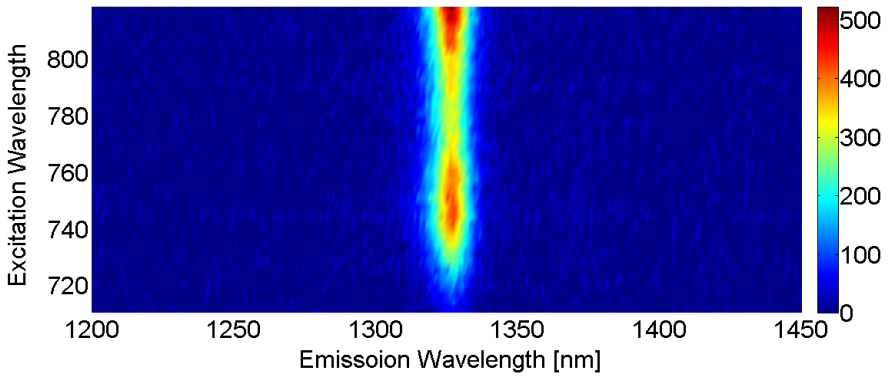

Fig. B.1.1: A PLE map in bundled SWCNTs.

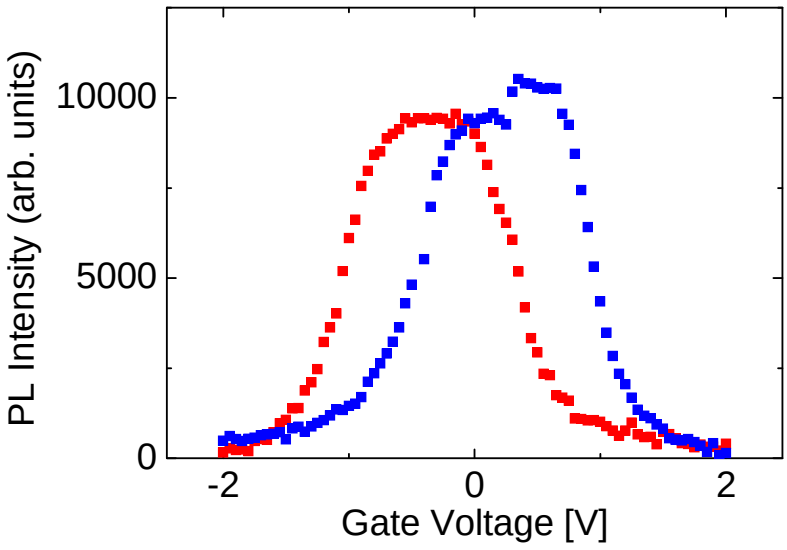

Fig. B.2.1: Gate voltage dependence of PL intensity changing gate voltage from -2 V to 2 V (red) and from 2 V to -2 V (blue)

References

[1] S. Iijima T. Ichihara, Nature **363**, 603 (1993).

[2] Ph. Avouris, M. Freitag, V. Perebeinos, Nat. Photonics **2**, 341 (2008).

[3] Ph. Avouris, Z. Chen, V. Perebeinos, Nat. Nanotech. **2**, 605 (2007).

[4] M. J. O'Connell, S. M. Bachilo, C. B. Huffman, V. C. Moore, M. S. Strano, E. H. Haroz, K. L. Rialonand, P. J. Boul, W. H. Noon, C. Kittrell, J. Ma, R. H. Hauge, R. B. Weisman, R. E. Smalley, Science **297**, 593 (2002).

[5] S. J. Tans, A. R. M. Verscheuren, C. Dekker, Nature **393**, 49 (1998).

[6] A. Javey, H. Kim, M. Brink, Q. Wang, A. Ural, J. Guo, P. Mcintyre, P. Mceuen, M. Lundstrom, H. Dai, Nat. Mater. **1**, 241 (2002).

[7] J. A. Misewich, R. Martel, Ph. Avouris, J. C. Tsang, S. Heinze, J. Tersoff, Science **300**, 783 (2003).

[8] J. Chen, V. Perebeinos M. Freitag, J. Tsang, Q. Fu, J. Liu, P. Avouris, Science **310**, 1171 (2005).

[9] T. Mueller, M. Kinoshita, M. Steiner, V. Perebeinos, A. A. Bol, D. B. Farmer, P. Avouris, Nat. Nanotech. **7**, 27 (2009).

[10] D. Mann, Y. K. Kato, A. K. Kinkhabwala, E. Pop, J. Cao, X. Wang, L. Zhang, Q. Wang, J. Guo, H. Dai, Nat. Nanotech. **2**, 33 (2006).

[11] N. M. Gabor, Z. Zhong, K. Bosnick, J. Park, P. L. McEuen, Science **325**, 1367 (2009).

[12] T. Ando, J. Phys. Soc. Jpn. **66**, 1066 (1997).

[13] F. Wang, G. Dukovic, L. E. Brus, T. F. Heinz, Science **308**, 838 (2005).

[14] S. Moritsubo, T. Murai, T. Shimada, Y. Murakami, S. Chiashi, S. Maruyama, Y. K. Kato, Phys. Rev. Lett. **104**, 247402 (2010).

[15] Y. Miyauchi, H. Hirori, K. Matsuda, Y. Kanemitsu, Phys. Rev. B **80**, 0814410 (2009).

[16] R. Matsunaga, K. Matsuda, Y. Kanemitsu, Phys. Rev. Lett. **101**, 147404 (2008).

[17] J. Lefebvre, J. M. Fraser, Y. Homma, P. Finnie, Appl. Phys. A. **78**, 1107 (2004).

[18] Y. Ohno, S. Iwasaki, Y. Murakami, S. Kishimoto, S. Maruyama, T. Mizutani, Phys. Rev. B **73**, 235427 (2006).

[19] Y. Ohno, S. Kishimoto, T. Mizutani, Nanotechnology **17**, 549 (2006).

[20] M. Steiner, M. Freitag, V. Perebeinos, A. Naumov, J. P. Small, A. A. Bol, P. Avouris, Nano Lett. **9**, 3477 (2009).

[21] A. V. Naumov S. M. Bachilo, D. A. Tsyboulski, R. B. Weisman, Nano Lett. **8**, 1527 (2008).

[22] R. Saito, G. Dresselhaus, M. S. Dresselhaus. *Physical Properties of Carbon Nanotubes*. Imperial College Press, (1998).

[23] H. Ajiki T. Ando, Physica B **201**, 349 (1994).

[24] J. Lefebvre P. Finnie, Phys. Rev. Lett. **98**, 167406 (2007).

[25] Y. Miyauchi, M. Oba, S. Maruyama, Phys. Rev. B **74**, 205440 (2006).

[26] S. Moritsubo. *Length dependence of photoluminescence from supended single-walled carbon nanotubes*. master thesis, The University of Tokyo, (2010).

[27] S. M. Bachilo, M. S. Strano, C. Kittrell, R. H. Hauge, R. E. Smalley, R. B. Weisman, Science **298**, 2361 (2002).

[28] R. B. Weisman S. M. Bachilo, Nano Lett. **3**, 9 (2003).

[29] R. Saito, G. Dresselhaus, M. S. Dresselhaus, Phys. Rev. B **61**, 2981 (2000).

[30] S. Reich C. Thomsen, Phys. Rev. B **62**, 4273 (2000).

[31] M. Ichida, S. Mizuno, Y. Tani, A. Saito, A. Nakamura, J. Phys. Soc. Jpn. **68**, 3131 (1999).

[32] J. Lefebvre, Y. Homma, P. Finnie, Phys. Rev. Lett. **90**, 217401 (2003).

[33] J. Lefebvre, J. M. Fraser, P. Finnie, Y. Homma, Phys. Rev. B **69**, 075403 (2004).

[34] J. Kong, H. T. Soh, A. M. Cassell, C. V. Quate, H. Dai, Nature **398**, 878 (1998).

[35] Y. Murakami, Y. Miyauchi, S. Chiashi, S. Maruyama, Chem. Phys. Lett. **377**, 49 (2003).

[36] J. Maultzsch, R. Pomraenke, S. Reich, E. Chang, D. Prezzi, A. Ruini, E. Molinari, M. S. Strano, C. Thomsen, C. Lienau, Phys. Rev. B **72**, 241402 (2005).

[37] G. Dukovic, F. Wang, D. Song, M. Y. Sfeir, T. F. Heinz, L E Brus, Nano Lett. **5**, 2314 (2005).

[38] V. Perebeinos, J. Tersoff, Ph. Avouris, Phys. Rev. Lett. **92**, 257402 (2004).

[39] Y. Miyauchi, R. Saito, K. Sato, Y. Ohno, S. Iwasaki, T. Mizutani, J. Jiang, S. Maruyama, Chem. Phys Lett. **442**, 394 (2007).

[40] O. Kiowski, S. Lebedkin, F. Hennrich, S. Malik, H. Rösner, K. Arnold, Phys. Rev. B **75**, 075421 (2007).

[41] A. G. Walsh, A. N. Vamivakas, Y. Yin, S. B. Croin, M. S. Ünlü, B. B. Goldberg, A. K. Swan, Nano Lett. **7**, 1485 (2007).

[42] Y. Ohno, S. Iwasaki, Y. Murakami, S. Kishimoto, S. Maruyama, T. Mizutani, Phys. Status Solidi (b) **244**, 4002 (2007).

[43] P. Finnie, Y. Homma, J. Lefebvre, Phys. Rev. Lett. **94**, 247401 (2005).

[44] R. Martel, V. Derycke, C. Lavoie, J. Appenzeller, K.K¿ Chan, J. Tersoff, Ph. Avouris, Phys. Rev. Lett. **87**, 256805 (2001).

[45] J. Appenzeller, J. Knoch, V. Dercke, R. Martel, S. Wijnd, Ph. Avouris, Phys. Rev. Lett. **89**, 126801 (2002).

[46] S. Heinze, J. Tersoff, R. Martel, V. Derycke, J. Appenzeller, Ph. Avouris, Phys. Rev. Lett. **89**, 106801 (2002).

[47] L Xie, H. Farhat, H. Son, J. Zhang, M. S. Dresselhaus, J. Kong, Z. Liu, Nano Lett. **9**, 1747 (2009).

[48] Z. Yao, C. L. Kane, C. Dekker, Phys. Rev. Lett. **84**, 2941 (2000).

[49] W. Kim, A. Javey, O. Vermesh, Q. Wang, Y. Li, H. Dai, Nano Lett. **3**, 193 (2003).

[50] L. Yang J. Han, Phys. Rev. Lett. **85**, 154 (2000).

[51] H. Maki, T. Sato, K. Ishibashi, Nano Lett. **7**, 890 (2007).

[52] T. K. Leeuw, D. A. Tsyboulski, P. N. Nikolaev, S. M. Bachilo, S. Arepalli, R. B. Weisman, Nano Lett. **8**, 826 (2008).

[53] M Freitag, M. Steiner, A. Naumov, J. P. Small, A. A. Bol, V. Perebeinos, Ph. Avouris, ACS Nano **3**, 3744 (2009).

[54] K. Matsuda, Y. Miyauchi, T. Sakashita, Y. Kanemitsu, Phys. Rev. B **81**, 033409 (2010).

[55] V. Perebeinos Ph. Avouris, Phys. Rev. Lett. **101**, 057401 (2008).

[56] S. Ilani, L. A. K. Donev, M. Kindermann, P. L. McEuen, Nat. Phys. **2**, 687 (2006).

[57] R. B. Capaz, C. D. Spataru, S. Ismail-Beigi, S. G. Louie, Phys. Rev. B **74**, 121401 (2006).

[58] C. D. Spataru, S. Ismail-Beigi, R. B. Capaz, S. G. Louie, Phys. Rev. Lett. **95**, 247402 (2005).

[59] V. Perebeinos, J. Tersoff, Ph. Avouris, Nano Lett. **5**, 2495 (2005).

[60] Y.-F. Xiao, T. Q. Nhan, M. W. B. Wilson, J. M. Fraser, Phys. Rev. Lett. **104**, 017401 (2010).

[61] L. Lüer, S. Hoseinkhani, D. Polli, J. Crochet, T. Hertel, G. Lanzani, Nat. Phys. **5**, 54 (2009).

List of publications and presentations

Publications

S. Yasukochi, T. Murai, S. Moritsubo, T. Shimada, S. Chiashi, S. Maruyama, Y. K. Kato, "Gate-induced blueshift and quenching of photoluminescence in suspended single-walled carbon nanotubes", in preparation.

Presentations

S. Yasukochi, T. Murai, T. Shimada, Y. Murakami, S. Chiashi, S. Maruyama, Y. K. Kato, " Electric field dependence of photoluminescence from individual single-walled carbon nanotubes ", March Meeting of the American Physical Society, Dalas, Texas (March 22, 2011).

T. Murai, S. Yasukochi, S. Moritsubo, T. Shimada, S. Chiashi, Y. Murakami, S. Maruyama, Y. K. Kato, "Photoconductivity measurements of single-walled carbon nanotube field effect transistors", March Meeting of the American Physical Society, Dalas, Texas (March 22, 2011).